AN ABSTRACT OF THE THESIS OF

Dane Michael Wiebe for the degree of Master of Science in Civil Engineering presented on March 22, 2013.

Title: Tsunami Inundation: Estimating Damage and Predicting Flow Properties

Abstract approved:

Daniel T. Cox

The 2004 Indian Ocean and 2011 Tohoku tsunami events have shown the destructive power of tsunami inundation to the constructed environment in addition to the tragic loss of life. A comparable event is expected for the Cascadia Subduction Zone (CSZ) which will impact the west coast of North America. Research efforts have focused on understanding and predicting the hazard to mitigate potential impacts. This thesis presents two manuscripts which pertain to estimating infrastructure damage and determining design loads of tsunami inundation.

The first manuscript estimates damage to buildings and economic loss for Seaside, Oregon, for CSZ events ranging from 3 to 25 m of slip along the entire fault. The analysis provides a community scale estimate of the hazard with calculations performed at the parcel level. Hydrodynamic results are obtained from the numerical model MOST and damage estimates are based on fragility curves from the recent literature. Seaside is located on low lying coastal land which makes it particularly sensitive to the magnitude of the events. For the range of events modeled, the percentage of building within the inundation zone ranges from 9 to 88%, with average economic losses ranging from $2 million to $1.2 billion.

The second manuscript introduces a new tsunami inundation model based on the concept of an energy grade line to estimate the hydrodynamic quantities of maximum flow depth, velocity, and momentum flux between the shoreline and extent

of inundation along a 1D transect. Using the numerical model FUNWAVE empirical relations were derived to tune the model. For simple bi-linear beaches the average error for the tuned model in flow depth, velocity, and momentum flux were 10, 23, and 10%, respectively; and for complex bathymetry at Rockaway Beach, Oregon, without recalibration, the errors were 14, 44, and 14% for flow depth, velocity, and momentum flux, respectively.

Tsunami Inundation: Estimating Damage and Predicting Flow Properties

by
Dane Michael Wiebe

A THESIS

submitted to

Oregon State University

in partial fulfillment of
the requirements for the
degree of

Master of Science

Presented March 22, 2013
Commencement June 2013

Master of Science thesis of Dane Michael Wiebe presented on March 22, 2013.

Approved:

Major Professor, representing Civil Engineering

Head of the School of Civil and Construction Engineering

Dean of the Graduate School

I understand that my thesis will become part of the permanent collection of Oregon State University libraries. My signature below authorizes release of my thesis to any reader upon request.

Dane Michael Wiebe, Author

ACKNOWLEDGEMENTS

Foremost, I express my appreciation to the Oregon Seas Grant whom funded this research. I also thank the ASCE7 subcommittee on Tsunami Loads and Effects for their input to the Energy Grade Line model; Christopher Moore and Yong Wei from PMEL who provided MOST/ComMIT training; and my committee members Yong Chen and Harry Yeh. I would also like to thank Yong Chen for providing the Clatsop County tax lot data. Lastly, I would like to express my gratitude to my advisor, Dan Cox, for his continual assistance and insight.

CONTRIBUTION OF AUTHORS

Dave Kriebel originated the idea of applying the Energy Grade Line (EGL) model for tsunami inundation, provided an example program for an idealized case, and provided several useful comments on this work. Hyoungsu Park performed the FUNWAVE simulations used for tuning the EGL model and later testing the application on a realistic shoreline. Dan Cox provided overall guidance for both papers and provided assistance with editing the manuscripts for publication.

TABLE OF CONTENTS

LIST OF FIGURES

LIST OF FIGURES (Continued)

LIST OF TABLES

Tsunami Inundation: Estimating Damage and Predicting Flow Properties

Introduction

The Cascadia Subduction Zone (CSZ) off the west coast of North America produces large magnitude earthquakes and tsunamis. Over the past 10,000 years there have been approximately 20 full length ruptures of the CSZ on the order of 8.9 M_W and approximately 25 partial ruptures on the order of 8.2 to 8.5 M_W (Goldfinger *et al.*, 2012). The average recurrence interval between CSZ events is 240 years, and the next event is estimated to have a 7-12% probability of occurrence in the next 50 years (Goldfinger *et al.*, 2012). The last full length rupture of the CSZ event occurred on 20 January 1700 and is estimated to have measured between 8.7 and 9.2M_W with 19 m of slip (Satake *et al.*, 2003). Although a large magnitude CSZ event is expected to happen at some point in the future, potential damage estimates are quite rudimentary.

Recent research efforts have focused on developing fragility curves to improve estimates of building performance to the tsunami hazard. While the concept of fragility curves is relatively new to the field of tsunami inundation, it has been widely applied to earthquake and flood hazards for decades. The difficulty in developing these functions for tsunamis is due to the scarcity of data and rarity of events. Nonetheless, recent fragility curves developed from the 2011 Tohoku tsunami were used to improve damage estimates at Seaside, Oregon, for a range of CSZ events.

To improve the resiliency of coastal communities to a CSZ event, critical infrastructure and facilities must survive and be functional. However, there is a lack of published design guidance and methods available to design engineers, who may lack time or resources to conduct full numerical inundation study, for estimating design loads from tsunami inundation. Therefore, a new tsunami inundation model based on the concept of an energy grade line was developed to estimate the hydrodynamic quantities of tsunami inundation.

Application of Fragility Curves to Estimate Damage and Economic Loss at a Community Scale: A Case Study of Seaside, Oregon

Dane M. Wiebe

Daniel T. Cox

Natural Hazards
Springer Science+Business Media

Van Godewijckstraat 30
3311 GX Dordrecht
Netherlands

To be submitted 2013

Abstract

Community scale estimates of damage and economic loss are modeled for Seaside, Oregon, for CSZ events ranging from 3 to 25 m of slip considering only the effects of the tsunami. Numerical simulations are obtained from the National Ocean and Atmospheric Administration's MOST model which includes a source model, subsidence, and calculation of the inundation flow characteristics. The damage estimates are based on fragility curves from the literature which relate flow depth with probability of failure for two different building classifications. Calculations are performed at the parcel level for the inundation hazard without including damage caused by the earthquake itself. Calculations show that Seaside is extreme sensitivity to the magnitude of the event because of its location on low lying coastal land. For the events modeled, the percentage of building within the inundation zone ranges from 9 to 88%, with average economic losses ranging from $2 million to $1.2 billion.

1.0 Introduction

Coastal Oregon communities are susceptible to two types of tsunamis: far-field and near-field. Far-field events, such as the 2011 Tohoku tsunami, pose relatively little danger to the Oregon coast. The first waves take several hours to arrive leaving enough time for most evacuations which limits loss of life. The waves are often too small to inundate large swaths of land and damage buildings. The highest damage potential from distant tsunamis it to bays and harbors, where increased currents can cause damage to docks and boats and can cause severe navigation hazards. In comparison, a local event generated from the Cascadia Subduction Zone (CSZ) is expected to cause widespread damage. The first waves are expected to arrive along the Oregon coast in the tens of minutes leaving little time for evacuation. Exacerbating this, intensive ground shaking from a local large magnitude earthquakes can last minutes, lowering evacuation times and damaging buildings. Fortunate for most coastal communities in the Pacific Northwest ground elevation quickly increases, providing safe evacuation zones. Communities such as Seaside, Oregon however, are built on particularly low land with safe ground beyond the extent of inundation hundreds of meters away. In these areas vertical evacuation is required.

The CSZ measures 1000 km in length and extends from the Mendocino Ridge off the coast of northern California to northern Vancouver Island (Figure 1). Along the CSZ the oceanic Juan de Fuca Plate is subduction beneath the continental North American Plate; however, due to friction the plates are locked together, preventing movement, and leading to an increase in stress and strain along the boundary (Geist, 2005). The strain deforms the plates, lowering the oceanic plate and raising the continental plate. Stress accumulates until it exceeds the frictional force and the plates slide past one another. At which time the strains in the oceanic and continental plates are suddenly released, resulting in a sudden uplift in the oceanic plate and a lowering of the continental plate (Stern, 2002). It is this sudden displacement of the oceanic plate which causes a perturbation of the water column from its equilibrium position and forms a tsunami.

The last great CSZ event occurred more than three centuries ago on 20 January 1700. It was a full length rupture extending from the Mendocino Ridge, off the coast of northern California, to mid-Vancouver Island, Canada. The event is estimated to have had a moment magnitude (M_W) between 8.7 and 9.2, and a slip of 19 m (Satake *et al.,* 2003). Over the past 10,000 years, the CSZ has shown three typical ruptures scenarios: a rupture of 200 – 450 km of the southern margin with 18-20 events on the order of 8.2 M_W, a rupture of 650 km starting at the southern margin with 3-4 events on the order of 8.5 M_W, and a full length rupture with 19-20 events on the order of 8.9 M_W (Goldfinger *et al.,* 2012). The average recurrence interval between CSZ events is 240 years, and the next event is estimated to have a 7-12% probability of occurrence in the next 50 years (Goldfinger et al., 2012).

To assses the hazard from the CSZ event, Gonzalez *et al.* (2009) developed probabilistic tsunami wave heights at Seaside, Oregon, for the 100 and 500 year events. The 100 year hazard is represented by a far-field Alaska-Aleutian event with wave heights less than 4 m. The 500 year hazard is represented by the near-field CSZ event with wave heights in excess of 10 m near the shoreline. As acknowledged by the authors, this paper does not include values of velocity or momentum flux which are better estimator of damage, and only includes the maximum wave height which can lead to under estimates of the tsunami hazard in some areas.

Wood (2007) investigated the tsunami hazard for coastal Oregon communities using graphical information software (GIS) and land use, population, and tax lot datasets. The work focused on providing a first step for developing mitigation, preparedness, response, and recovery strategies. Aggregate quantities of assets within the inundation zone were totaled to determine the community's exposure level, and compared to the total assets to determine the sensitivity. The work identified Seaside, Oregon, as the most vulnerable to the tsunami hazard in terms of exposure and sensitivity. The work treated the assets inside and outside the inundation line binarily, and did not account for the spatial variation in the hazard.

Dominey-Howes *et al.* (2010) improved on Wood's approach by accounting for the spatial variation in the hazard. Again, the region of interest was Seaside, Oregon, and the authors used the 500 year tsunami event from the Seaside Pilot Study (Tsunami Pilot Study Working Group, 2006) and Clatsop County tax lot data as input into the Papathoma Tsunami Vulnerability Assessment (PTVA) model to estimate probably maximum loss. The model was quite extensive in that it accounts for various aspects of the hazard such as flow depth, building row from the sea, building material, number of stories, orientation, building condition, surroundings, and land cover; however, the vulnerability score is calculated by a summation of the standardized scores multiplied by a weighting coefficient. The problem with this approach arises from assigning an appropriate weighting coefficient to each criterion. For this study the authors state that the values are based on expert judgment, but the values appear to be somewhat arbitrary, linearly decreasing from 8 to 1. Accounting for all of these variables is ambitious, but perhaps superfluous considering the variability in the hazard. The authors acknowledge a lack of credible fragility curves available at the time of this study, and mention that these curves could be incorporated into the PTVA model as they become available.

To aid future policy and planning efforts a probabilistic estimate of damage and economic loss for Seaside, Oregon, from CSZ events are examined. This paper presents community scale damage estimates from locally generated CSZ tsunami for Seaside, Oregon. Section 2 covers the hazard, which includes introducing the numerical mode MOST, the range of CSZ events modeled, and analysis of hydrodynamic results. Section 3 covers the damage estimate, which includes introducing the fragility curves, the tax lot dataset, and analysis of the sensitivity of the hazard and damage estimates with respect to the event magnitude. Section 4 summarizes key findings and suggests future research.

2.0 Numerical Model Simulations

The numerical simulation model Method Of Splitting Tsunamis (MOST) developed by Vasily Titov from the Pacific Marine Environmental Laboratory (PMEL) of the National Oceanic and Atmospheric Administration (NOAA), and by Costas Synolakis from the University of Southern California is used to model a series of tsunami events at Seaside, Oregon. MOST is a finite difference model, based on the depth integrated non-linear shallow water wave equations, accounts for wave dispersion, includes a Manning's term for friction, and uses a set of three nested grids (PMEL, 2006; National Tsunami Hazard Mitigation Program, 2012). The model proceeds in three distinct phases: deformation, propagation, and inundation. The deformation phase provides the initial hydrodynamic tsunami parameters for a specified event and is based on the Okada deformation model (Okada, 1985). All of the major subduction zones around the world have been delineated by PMEL into 50 x 100 km tiles, which act as unit sources, and include the strike, dip, and rake angles, and the depth of the epicenter, which are used to calculate the slip distance for a given magnitude event. The propagation phase uses the non-linear shallow water wave equations to propagate the waves generated by the deformation across the oceans to the shoreline. The inundation phase uses a 1D algorithm, derived from the Vasily Titov Costas Synolakis (VTCS) model (Titov & Synolakis, 1995), to move the shoreline position based on a horizontal projection of the water level. Further information regarding the governing equations, numerical implementations, and validation can be found in Titov & Synolakis (1998), PMEL (2006), and Tang *et al.* (2009).

Community Model Interface for Tsunami (ComMIT) is a java program which provides a graphical user interface to run MOST. It also provides access to a database of pre-computed tsunami events for each 50 x 100 km unit source (http://sift.pmel.noaa.gov/data). Using this propagation database, tiles representing the fault of interest are selected, and the magnitude of the event is specified. ComMIT accesses the shared database and generates the initial, and boundary conditions for the

grids. Further details of ComMIT and the propagation database are available in Titov *et al.* (2011) and Gica *et al.* (2008).

2.1 Digital Elevation Models (DEM)

DEM data for this study was obtained from high-resolution DEMs provided by the National Oceanic and Atmospheric Administration and National Geophysical Data Center. The DEMs included: Astoria, OR, Garibaldi, OR, Seaside, OR, and the NW Pacific Coast. The Seaside DEM is referenced to mean high water (MHW), with a spatial resolution of 1/3 arc-second, approximately 10 m, and was sub-sampled for the C grid. The Astoria and Garibaldi DEM's are also referenced to MHW, with a spatial resolutions of 1/3 arc-second and were sub-sampled for the B grid. The NW Pacific Coast DEM is referenced to mean sea level (MSL), with a spatial resolution of 3 arc-second, and was sub-sampled for the A grid. Table 1 lists the details, extent, and resolution of each grid, and Figure 2 shows the details and extents.

2.2 Modeled Events

Earthquake intensity is commonly reported in terms of moment magnitude, M_W, which is a measure of energy based on the seismic moment, M_0 (Hanks & Kanamori, 1979):

$$M_W = \frac{2}{3}\log_{10} M_o - 10.7 \tag{1}$$

where the seismic moment is calculated by:

$$M_o = \mu AD \tag{2}$$

where μ is the shear modulus of the fault material, A is the area displaced, and D is the displacement, known as the slip distance. Every unit increase in M_W represents a 31.6 fold increase in energy. Over the past 10,000 years full length CSZ events have ranged from 8.7 to 9.1 M_W (Goldfinger *et al.*, 2012) which correspond to a 13 fold increase in energy.

For these full length ruptures the displaced area remains relatively constant (Goldfinger et al., 2012), so the increased energy acts to increase the slip distance. Slip is the displacement distance between two plates on either side of a fault relative one another. For subduction zone earthquakes, slip is a main mechanism in determining the magnitude of a tsunami. Other key parameters include the displaced area, the fault type, and the angles at which the displacement occurs. Figure 3 shows the sensitivity of the slip as a function of M_W for rupture lengths ranging from 400 to 1200 km. In all cases the rupture width is 100 km for equivalent rupture areas of 40,000 to 1,200,000 km^2. For constant 9.0 M_W events with rupture lengths of 400 and 1200 km the corresponding slip distances are 22.2 and 7.4 m, respectively, a 3 fold decrease. The calculated slip distances of a few recent and historically significant events are also plotted on this figure. Note there is uncertainty in the estimated moment magnitudes and rupture lengths due to fault asperities. The historical values were taken from Yoshida *et al.* (2011), Delouis *et al.* (2010), Hirata *et al.* (2006), Ichinose *et al.* (2007), and Satake *et al.* (2003).

For this paper, a full length CSZ rupture (100 km wide by 1000 km long) is modeled from the Mendocino Ridge, CA, to Vancouver Island, BC. Five simulated tsunami events ranging from 8.7 to 9.3 M_W are modeled using the numerical model MOST. Table 2 lists the details of each simulated event. For these events the slip distance ranges from 3.15 to 25.00 m. Figure 4 shows the deformation from a hypothetical 9.0 M_W earthquake, with a rupture length and width of 1000 and 100 km, respectively. Over this area the average strike and dip angles are 345 and 10 degrees, respectively. At the fault the maximum uplift is 3.4 m, and along the coast the maximum subsidence is 1.5 m. The extents of the grids A, B, and C are also shown in the figure.

2.3 Numerical Results

Figure 5 shows the maximum extent of inundation for the five modeled events. The extent of inundation is sensitive to slip, which is directly related to M_W since the

displaced area is held constant for this work. For 3 m of slip, the extent of inundation closely resembles the existing shoreline (blue line) and it does not overtop the first peninsula formed by the Nencanicum River. The 6 m slip event (green line) inundates the first peninsula but does not inundate the second half of the city between the Necanicum River and Neawanna Creek. The 9 m slip event (yellow line) inundates most of the low lying portion of Seaside. The 13 and 25 m slip events increase the extent of inundation to the base of the small coastal mountain range. The white box in Figure 5B highlights a section of detail that will be used in later figures.

Figure 6 show a time series of the offshore wave amplitude at the 10 m bathymetric contour for four hours for the 5 events. The wave amplitude is defined as the vertical displacement of the free surface referenced to mean high water (MHW). The location of the wave gage is shown in Figure 5A. For all 5 events the maximum wave amplitude is associated with the first wave and reaches the shoreline in approximately 35 minutes. The maximum wave amplitude at the location of the wave gage for the 3, 6, 9, 13, and 25 m slip events are 1.9, 3.7, 5.1, 7.0, and 12.2 m, respectively.

Figure 7 shows the maximum values of the wave amplitude or flow depth, velocity, and momentum flux for the13 m slip event for the C grid. In this paper, all figures relating to the free surface report the wave amplitude for offshore values and flow depth for onshore values. The flow depth is defined as the vertical distance from the land elevation to the free surface elevation. At the shoreline, the boundary between these two regions, the wave height and flow depth are equal by definition. The momentum flux per unit mass per unit width is defined as a flow depth multiplied by a squared velocity and is sometimes termed the specific momentum flux. In this paper, we retain ‘momentum flux’ for brevity. The maximum momentum flux is the peak of the momentum flux time series, and it is noted that the flow depth and velocity associated with the momentum flux are less than either the maximum values of flow depth or velocity for a given event. For the a 13 m slip event the maximum offshore

wave amplitude, velocity and momentum flux near the shoreline reach values as high as of 8 m, 10 m/s, and 200 m^3/s^2.

Figure 8 shows the detailed maximum values of flow depth, velocity, and momentum flux for the 13 m slip event for the region represented by the white box in Figure 5A. The dimensions are 450 m east-west by 600 m north-south and indicate one of the main commercial centers of Seaside. The black dotted lines represent the road network, and circle is used to indicate the roundabout at the end of Broadway Street marking a main thoroughfare running perpendicular to the shoreline. Along the western most road near the circular roundabout the flow depth decreases from 8 to 3 m, while the velocity and momentum increases from 4 to 8 m/s and from 75 to 150 m^3/s^2, respectively. There are other maximum velocity and momentum flux hotspots which vary spatially from the maximum flow depth locations. This highlights the need and importance of understanding how building failure can be estimated from flow depth, velocity, or momentum flux (Yeh *et al.*, 2005; FEMA, 2008). For example, Figure 8C shows a hotspot of momentum flux along the first east-west street below the roundabout whereas Figure 8A and 8B do not show the same hotspot patter in this region. Therefore, damage predictions based solely on flow depth, velocity, or momentum flux would give markedly different results. It is noted that the calculations assume a bare earth DEM model, and the influence of the macro-roughness or large buildings is not included (Park *et al.*, submitted; Rueben *et al.*, 2011; Cox *et al.*, 2008).

Figure 9 shows the maximum flows depths associated with the 6, 9, and 13 m slip events. The overall trend of high and low values remain constant as the magnitude of the event increases, but the average flow depths over the domain increases from 1.5 to 2.9 to 4.7 m, respectively. Due to the logarithmic scale of the seismic moment a 0.1 increase in magnitude results in approximately 3 m increase in slip, and 1.5 m increase in flow depth for the cases shown.

3.0 Method of Damage Estimation

Damage estimates were derived from fragility curves published in the literature. A fragility curve is a statistical function which describes the performance (or damage state) for a given demand (or loading condition). The curves are typically S-shaped, which describes the uncertainty in the system's capacity to withstand a loading condition (Schultz *et al.*, 2010). For example, a gradual curve implies a high uncertainty in the performance for a given demand, whereas a steep curve implies a high certainty in the performance. Fragility curves with high uncertainty may lead to an under prediction of performance at low demands, and over prediction of performance at high demands (Schultz *et al.*, 2010). There are typically four methods used to develop fragility curves: judgmental, empirical, analytical, and hybrid (Schultz *et al.*, 2010).

For tsunami performance, fragility curve have typically been developed using an empirical approach of field observations, laboratory experiments, and numerical simulations (e.g. Koshimura *et al.*, 2009). An advantage of using fragility curves is that they incorporate all of the hazards and uncertainty into a single function; however, extreme care must be taken to ensure that the fragility functions are appropriate for the intended application. For example, fragility curves developed by Koshimura *et al.* (2009), Suppasri *et al.* (2011), and Murao & Nakazato (2010) from the 2004 Indian Ocean tsunami for Indonesia, Thailand, and Sri Lanka would be inappropriate for application along the Oregon coast for a CSZ event or other areas with different building standards as suggested by the these authors. First, the construction quality and build standards in the U.S. are different than those in developing countries. Therefore, the performance under the same loading condition is expected to be different. Second, the curves developed for regions far from the epicenter; such as Sri Lanka, do not include the near-field earthquake hazard. Park *et al.* (2012) have shown a numerical approach of combining the probabilistic seismic and tsunami hazards. Recent fragility curves developed from the 2011 Tohoku event are the most appropriate for our application (e.g. Suppasri *et al.*, 2012).

Figure 10 shows the fragility curves developed by Suppasri *et al*. (2012) from the 2011 Tohoku event which are used in this study. These curve have the advantage of providing four performance levels ranging from minor to complete damage for both wooden and concrete/steel buildings. Table 3 lists descriptions of the severity of minor, moderate, major, and complete damage. A limitation of theses fragility curves are that they are all based on the flow depth, and fagility curves for velocity and momentum flux from the 2011 event have yet to be developed. These curves show an initiation of probabilities of damage for flow depths around 1 m, and complete damage beyond 7 m.

Damage estimates are performed on the parcel level. Tax lot data collected by the Clatsop County Assessor of the Assessment and Taxation Department were used to obtain information on each parcel. Each parcel is categorized with a three digit property classification which is used to assign a building type (wooden or concrete/steel). As a simplifying assumption, all residential structures are taken as wooden and all commercial structures are taken as concrete/steel. Based on several site visits, this assumption is reasonable, particularly for residential buildings which are nearly all wood and for large, newer hotels which typically have modern construction. Some of the older, smaller hotels and small businesses are a mix of wood and concrete construction. The assignment of building type could be refined by performing a more detailed field survey and assigning types individually or assigned probabilistically based on a percentage of buildings types. However, this second approach would introduce a random spatial distribution which would require statistical analysis (e.g. Monte Carlo simulation). The real market value (RMV) of each parcel is divided into land value and building value. For this analysis, only the building values were used as we are interested in damage/replacement cost.

Figure 11 shows aerial imagery, building type, and building value for downtown Seaside. The shoreline is fronted by large hotels, the north landward area is

a commercial district, and the south area is manly residential dwellings (gray shaded building in Figure 11C).

3.1 Estimate of Damage

Figure 12 shows the probability of moderate damage for the 9, 13, and 25 m slip events by applying the fragility analysis to the building types assumed from the tax lot data and the flow depths estimated by MOST. The damage patterns in Figure 12A directly correlate with the flow depth patterns Figure 9C. The only differences are lower probabilities of damage in the northern commercial area in comparison to the southern residential area due to increased performance of concrete/steel buildings over wooden buildings. The probability of moderate damage increases significantly between these events. For the 9.0 m slip event most of the buildings have less than 50% probability of moderate damage, whereas for the 25 m slip event the probability increases to greater than 75%.

Figure 13 shows the probabilities of moderate, major, and complete damage for the 13 m slip event. The majority of the buildings have a probability of moderate damage greater than 75%, but a probability less than 50% for complete damage. The spatial scatter of probability of damage shown in this figure is similar to the level of scatter shown in the vulnerability score of Dominey-Howes *et al.* (2010).

As mentioned previously, the DEMs used to compute the hydrodynamics are bare earth models and do not account for the spatial sheltering afforded by other buildings which may lower damage estimates, or accelerate flows between building which may increase damage estimates. Numerical modelling of tsunami inundation for constructed environments has been successful performed and verified by physical laboratory studies (e.g. Park *et al.* (submitted)). However using the hydrodynamics for communitee scale damage estimates introduces new challenges due to the temporal variation in building failure which would need to be incorporated into the DEM to properly model the hydrodynamics and the debris field which may change the severity of damage in some areas (Cercone *et al.*, submitted).

Table 4 lists the number of building within the inundation zone for the five modeled events, the number of buildings with greater than 25, 50, and 75% probabilities of moderate damage, and the number of buildings with minor, moderate, major and complete damage with probabilities of occurrence greater than 50%. Within the study area (C grid) there are a total of 10,043 buildings. Comparing the number of buildings with moderate damage for probabilities greater than 25, 50, and 75% for the 9 and 13 m slip events shows the sensitivity of damage. For the 9 m slip event there is a decrease of 45 and 53% in the number buildings impacted between probabilities greater than 25 and 50%, and 50 and 75%, respectively, for the 13 m slip event the decrease is only 14 and 25%, respectively. This indicates that the average probability of damage is increasing even though more buildings are being inundated.

Some of the data listed in Table 4 are plotted in Figure 14. Figure 14 shows the number of buildings with probabilities of occurrence greater than 50% for minor, moderate, major, and complete damage for 3, 6, 9, 13, and 25 m slip events. This figure illustrates the sensitivity of damage for Seaside to events near 9 m of slip. For 6 m of slip relatively few buildings are expected to be damage. Only 2.3% of buildings have probabilities of minor damage above 50%. For 13 m of slip 53% of buildings have probabilities of minor damage above 50%.

For this paper only the direct tangible economic loss was tabulated, which is damage to buildings. Direct intangible loss, such as loss of life, and indirect tangible loss, such as the disruptions to the regional economy, were not considered. It is noted that the tax lot data included information on the land value and the improved value. Only the improved value (value of the structure) was used and did not include assets to business (e.g., dry goods or furnishings) inside the buildings.

There are multiple ways to calculate the economic loss using the probabilities of damage and the real market value (RMV) of the building from the tax lot dataset. A few methods are listed below (the list is by no means exhaustive):

Method 1) Aggregates a percentage of the RMV for all buildings with probabilities greater than zero.

$$E_{Loss} = \sum RMV \times P$$

Method 2) Aggregates the full RMV for all buildings with probability of damage greater than a threshold of 50%.

$$E_{Loss} = \sum RMV \quad if\ P > 50\%$$

Method 3) Aggregates a percentage of the RMV based on the probability of damage for three damage states.

$$E_{Loss} = \sum \frac{RMV}{3}\left(P_{Minor} + P_{Moderate} + P_{Major}\right)$$

Table 5 lists the probable cost for 3, 6, 9, 13, and 25 m slip events and four damage levels using the three methods presented above. Within the study area (C grid) the total RMV of all assets totals $1.5 billion.

Figure 15 shows the probable cost estimated using methods 1, 2, and 3 for minor, moderate, major, and complete damage for 3, 6, 9, 13, and 25 m slip events. Similar to Figure 14 this figure illustrates the sensitivity of damage for Seaside to events near 9 m of slip. For 6 m of slip the probable loss is estimated to total between $2.4 and $45.8 million, and for 13 m of slip is estimate to total between $166.9 and $742.4 million. As a percentage of the total RMV of all assets within the study area the range of probable cost for 6 and 13 m slip events are 0.2 to 3.1% and 11.4 to 50.7%, respectively.

For 17 of the 20 cases, Method 1 provided a higher estimate of loss in comparison to Method 2, and in those 3 cases the difference was less than 6%. The highest discrepancy in terms of percentage between methods 1 and 2 is for the 3 and 6 m slip events where relatively little damage is expected. The highest discrepancy for the larger events was 33% which was for the estimate of complete damage for the 13 m slip event. This is most likely attributed to a large number of buildings with probabilities of complete damage just below 50%. Method 3 assigns an equal

weighting to the probabilities of minor, moderate, and major damage and provides an average loss estimate in comparison to the other curves.

Table 6 lists a summary comparing the methods and results of Wood (2007) and Dominey-Howes *et al.* (2010) with this study. The "379 Line" which refers to the line of maximum inundation used by the State of Oregon for planning purposes was used as the extent of inundation in Woods (2007). The "379 Line" extent of inundation is most similar to the 13 m slip event modeled by MOST for this paper. The probabilistic 500 year event used by Dominey-Howes *et al.* (2010) based on the NOAA study is most similar to the 6 m slip event in comparison to the inundation extent and the 13 m slip event is comparison to flow depths modeled by MOST in this paper. As expected comparing the total value of assets within the inundation zones provide similar results. The estimated loss however, is markedly different. Dominey-Howes *et al.* (2010) aggregated the full RMV of all buildings with "vulnerability class" medium-high and high and did not include any values for building of lower "vulnerability class". In the PTVA model used by Dominey-Howes *et al.* (2010) the flow depth had the highest weighting on the vulnerability score, so comparison with the 13 m slip event is more appropriate than comparison with the 6 m slip event. The difference in the value of assets within the extent of inundation between the probabilistic 500 year event and the 13 m slip event is $268 million, and the difference in the estimated loss between Dominey-Howes *et al.* (2010) and this study using fragility curves is $416 million, for an increased estimated loss of $148 million for this study. Although the estimated loss by Dominey-Howes *et al.* (2010) is reasonable and falls within the bounds of the 6 to 13 m events, the PTVA model lacks the physics based approached of fragility curves. Similar to Dominey-Howes *et al.* (2010) improving on Woods (2007) work by incorporating the spatial variability of the hazard, this work improves on Dominey-Howes *et al.* (2010) work by incorporating fragility curves.

This paper provides a methodology for the application of fragility curves to estimate building damage on a community scale. The estimates provided in the paper could be improved by refining the building classification using recently published fragility curves by Suppasri *et al*. (2013). These new curves are developed for wood, steel, reinforce concrete, masonry, and mixed building materials for 1, 2, and 3 storey buildings. The damage estimates could also account for key infrastructures such as roads, bridges, and utilities (water/wastewater, power, gas, telecommunication networks), which are critical to community recovery. Other aspects which are important to include but hard to measure are damage to farmlands and ecosystems.

4.0 Conclusions

A community scale estimate of damage and economic loss calculated at the parcel level was performed for Seaside, Oregon, using fragility curves from the literature for events ranging from 3 to 25 m of slip. The numerical model MOST was used to obtain hydrodynamic values, and tax lot data used to determine building type and value. Primary conclusions are:

1. For the first time fragility curves were applied to Seaside, Oregon to estimate probable damage states for a range of CSZ events. Seaside was found to be sensitive to the magnitude of the events, with minor damage expected for events less than 9 m of slip and severe damage expected for events greater than 9 m of slip. This sensitivity is due the community being situated on low lying coastal lands.
2. For the 3, 6, 9, 13, and 25 m slip events the percentage of buildings within the inundation zone are 9, 45, 59, 66, and 88%, respectively, with an average economic loss ranging from $2 million to $1.2 billion.
3. Based on the hydrodynamic results, using fragility curves based solely on the flow depth may lead to an underestimate of damage, and a need exists for fragility curves as function of momentum flux to be developed.

Future work should include the development of fragility curves based on velocity and momentum flux, to provide a better estimate of damage. For economic loss, future work should include economic input/output models to calculate the indirect tangible losses to the regional economy. The probabilities of each modeled event could also be related to the damage estimates, similar to the probabilistic hazard from the Seaside pilot study (Tsunami Pilot Study Working Group, 2006), to provide a probabilistic damage estimate.

Acknowledgements

This work was funded by the Oregon Sea Grant.

Figures

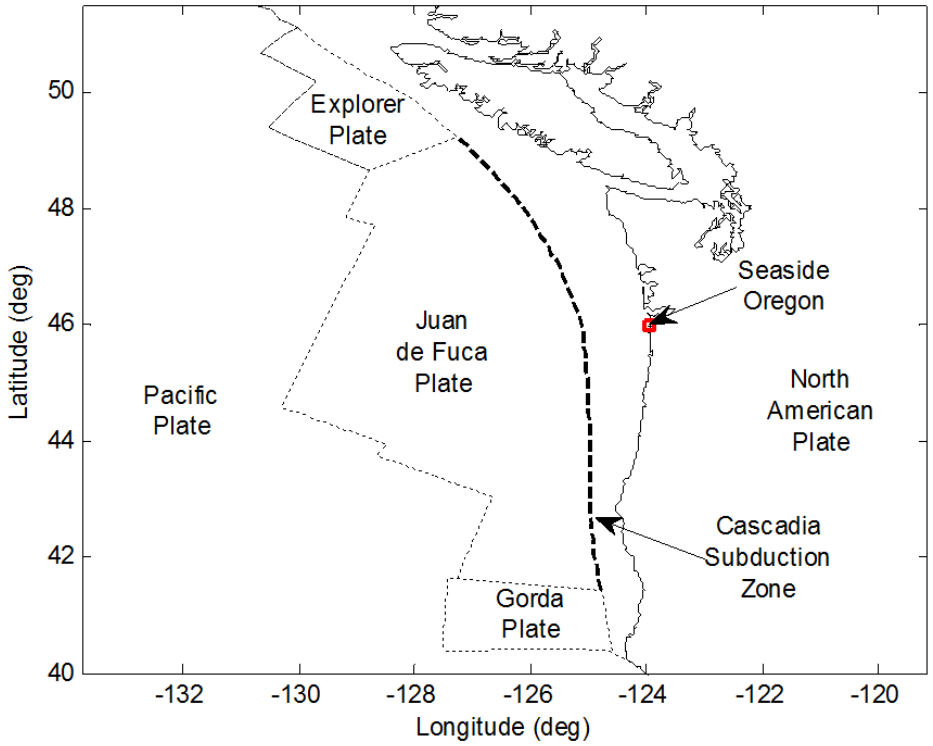

Figure 1 Regional map of study area showing the Cascadia Subduction Zone.

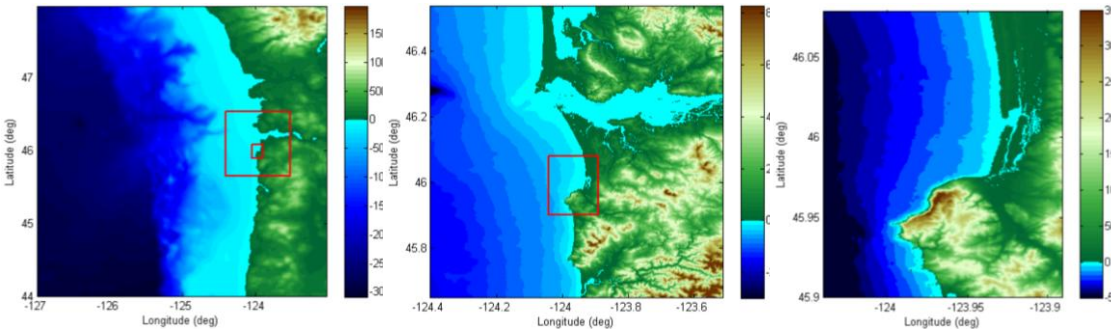

Figure 2 Digital elevation models for grids A (left), B (middle), and C (right). The boxed regions within grid A and B represent the regions of grids B and C.

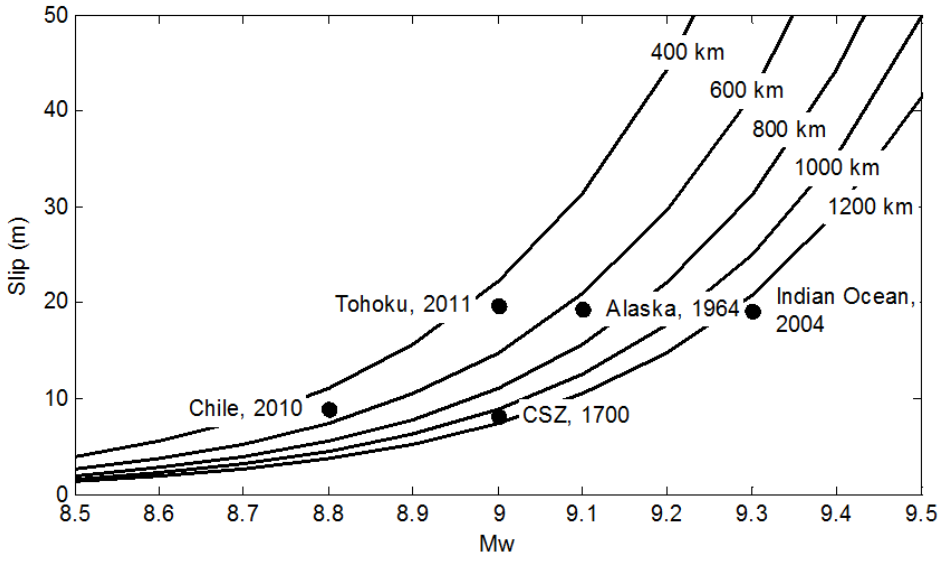

Figure 3 Fault slip as a function of earthquake magnitude for various rupture length, and notable historic event.

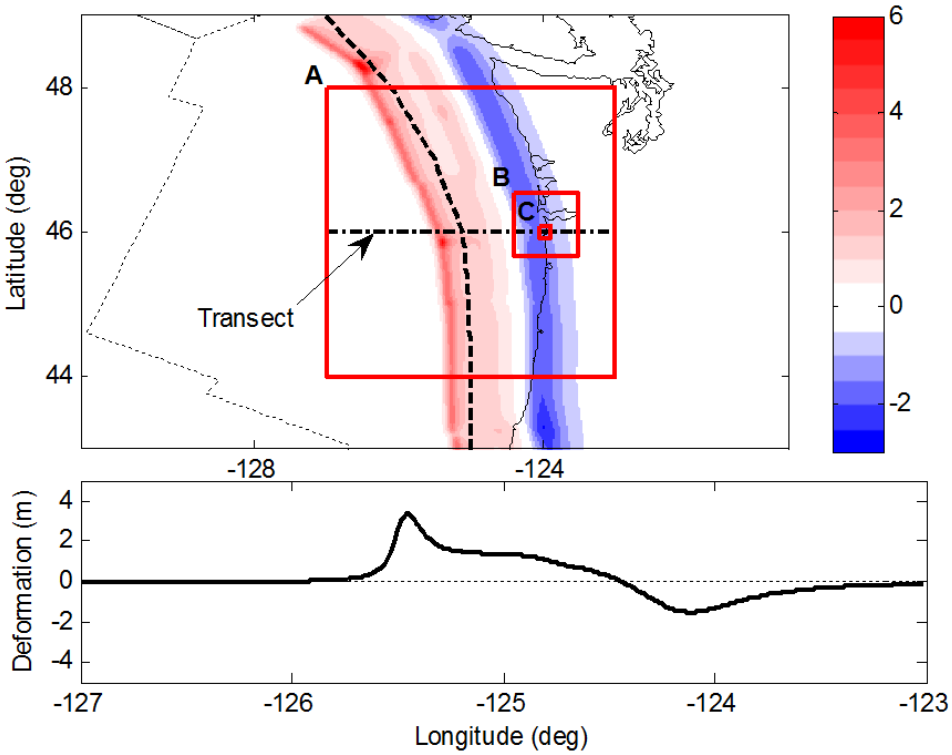

Figure 4 Deformation along the CSZ from a 9.0 M_W event for a 1000 km by 100 km rupture.

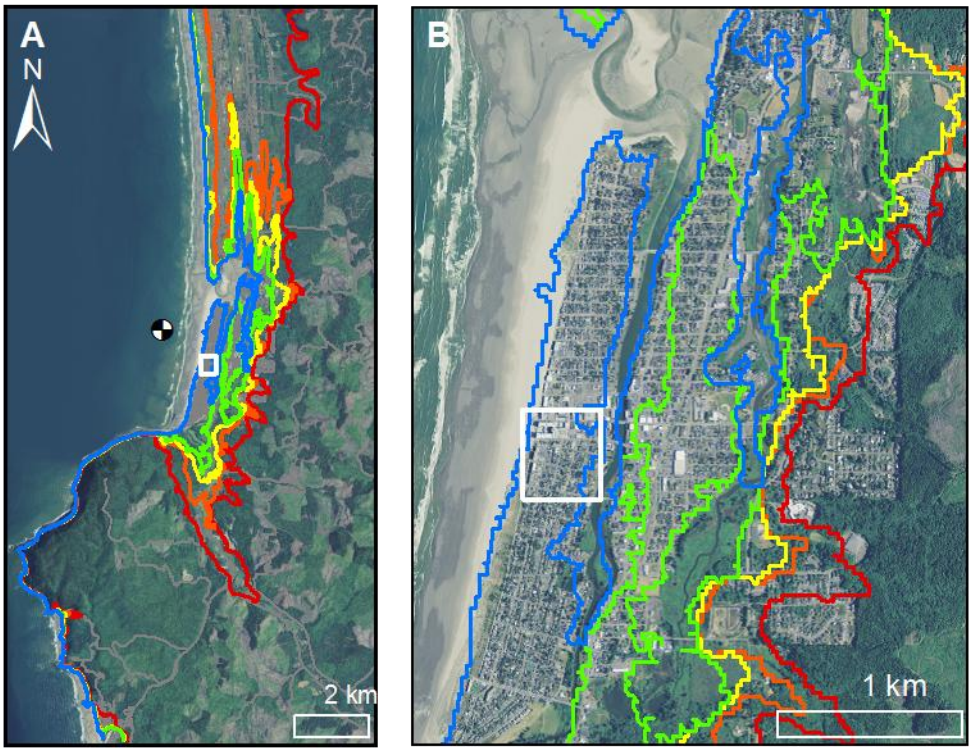

Figure 5 Regional plan view (A) and community plan view (B) of the maximum extent of inundation for the five modeled events. The white box bounds the downtown region which is examined in detail. The Secchi disk in panel A is the location of a virtual wave gage for Figure 6. Slip = 3 (blue), 6 (green), 9 (yellow), 13 (orange), and 25 m (red).

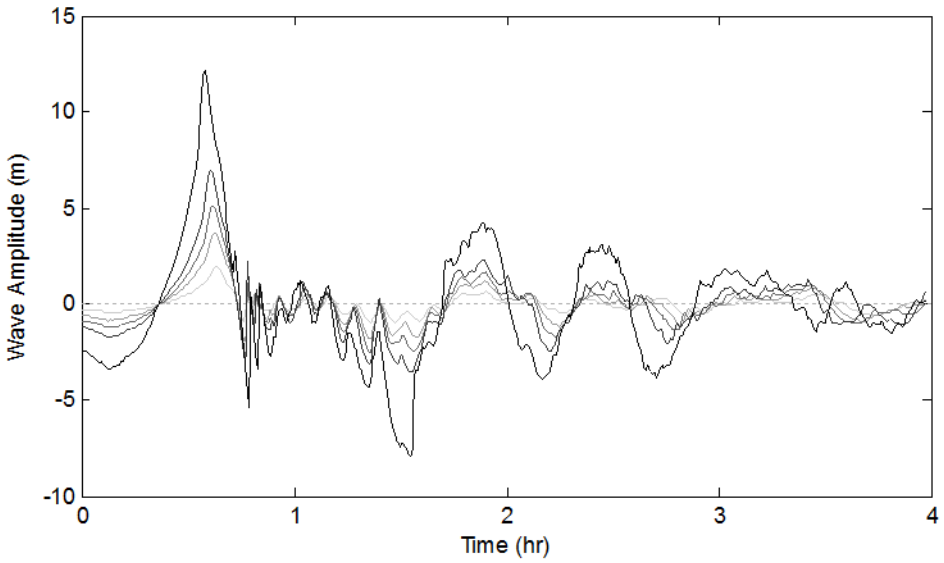

Figure 6 Time series of the offshore wave height at the 10 m contour for the 3, 6, 9, 13, and 25 m slip events (gray to black lines). The location of the wave gage is shown in Figure 5A.

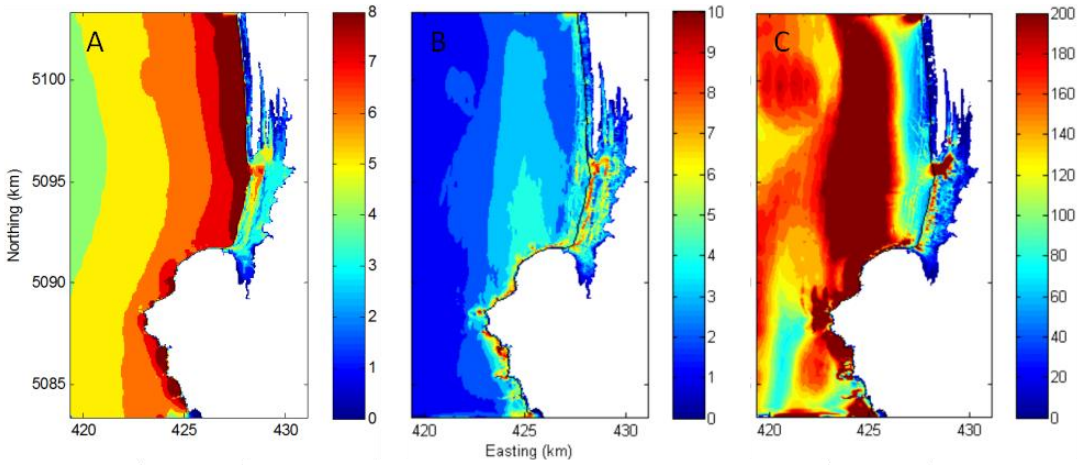

Figure 7 Maximum values of (A) wave height and flow depth (B) velocity and (C) momentum flux in the C grid of MOST for a 13 m slip event.

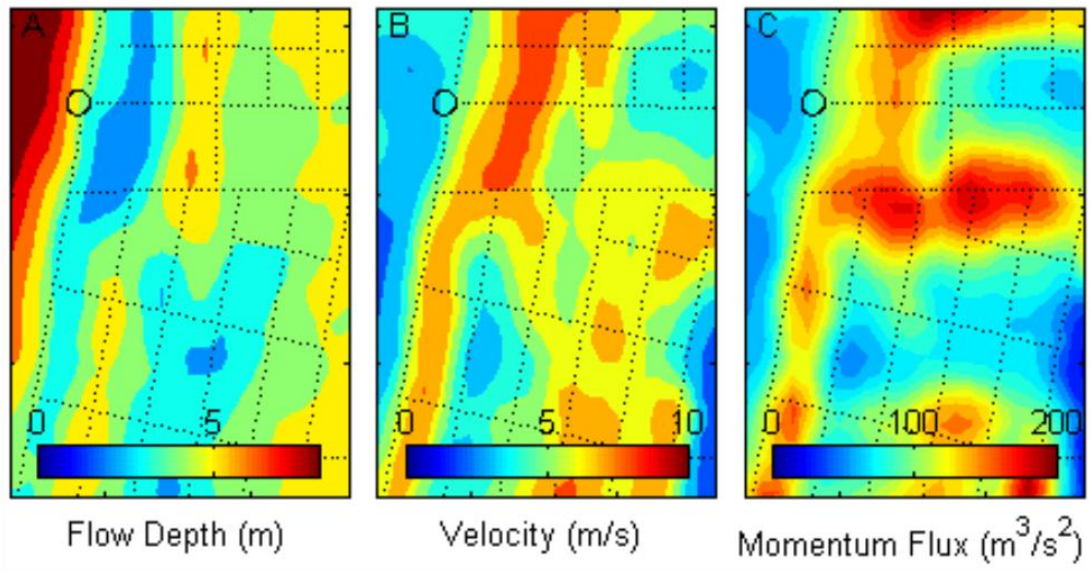

Figure 8 Maximum values of (A) flow depth (B) velocity and (C) momentum flux in downtown Seaside for a 13 m slip event. Road network (dotted lines).

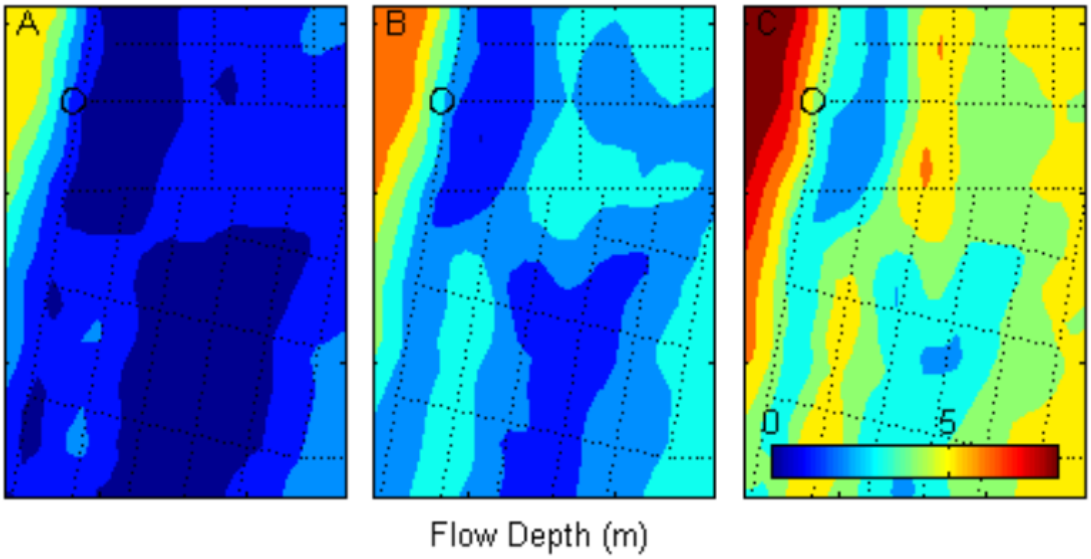

Figure 9 Maximum flow depths in downtown Seaside for slip = 6 (A), 9 (B), and 13 m (C). Road network (dotted lines).

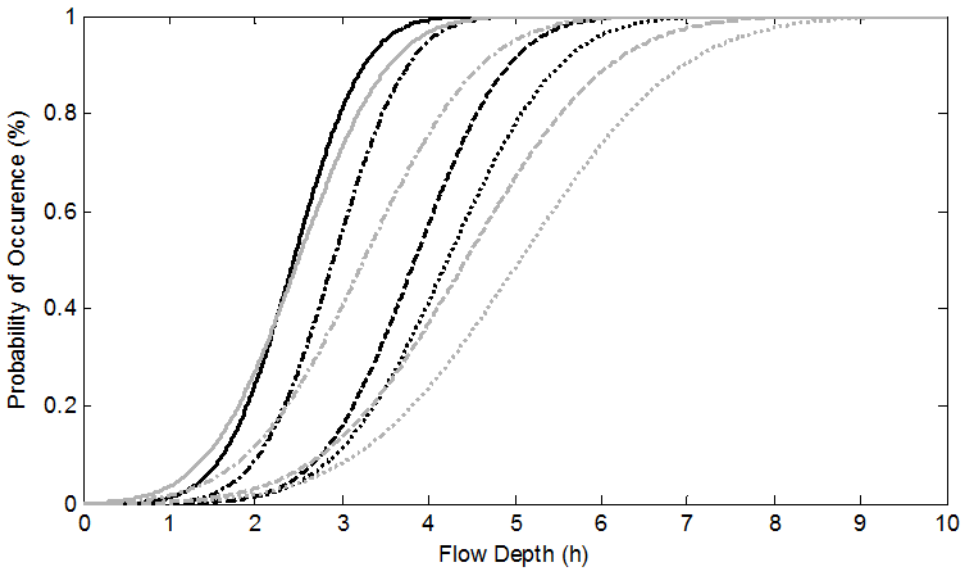

Figure 10 Tsunami fragility curves for damage levels to wooden house and concrete/steel buildings as a function of flow depth. Minor damage (solid), moderate damage (dashed dotted), major damage (dashed), and complete damage (dotted), wooden houses (black) and concrete/steel buildings (gray). Data re-plotted from Suppasri *et al*. (2012).

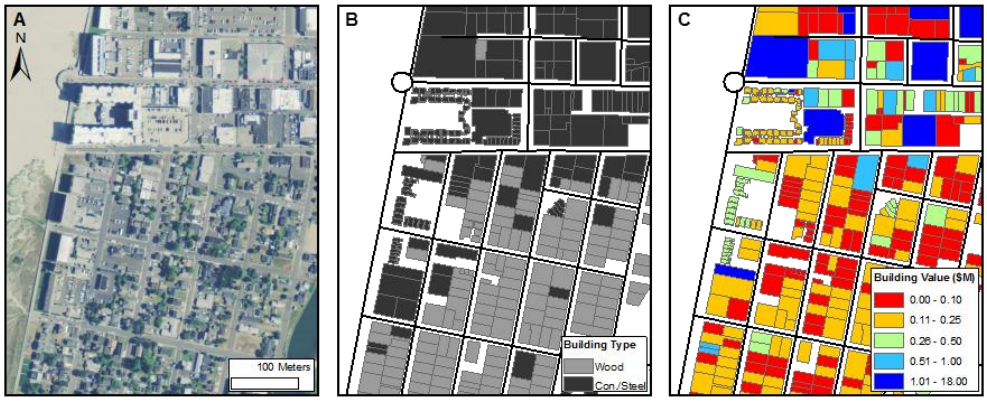

Figure 11 Downtown Seaside: Ariel imagery (A), construction type (B), and building value (C).

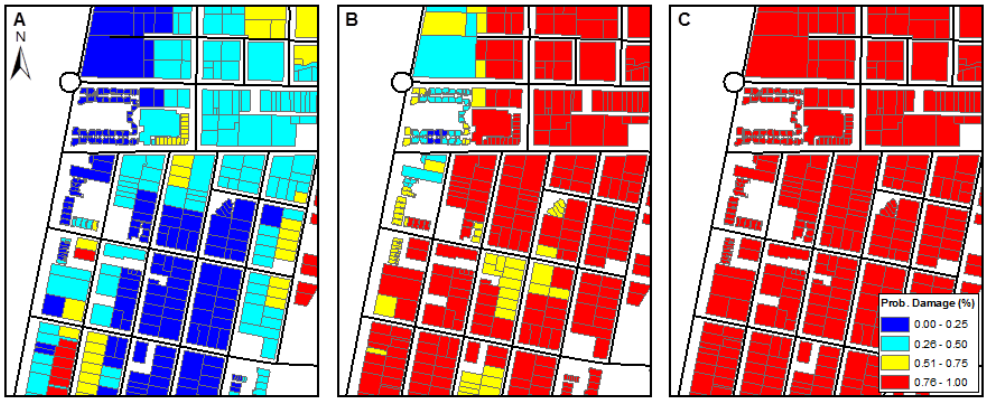

Figure 12 Probability of moderate damage for slip = 9 (A), 13 (B), and 25 m (C).

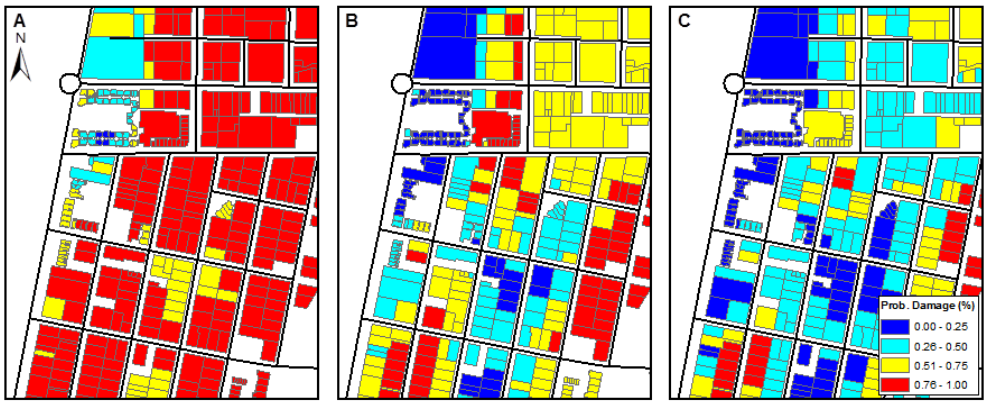

Figure 13 Probability of moderate (A), major (B), and complete (C) damage for slip = 13 m.

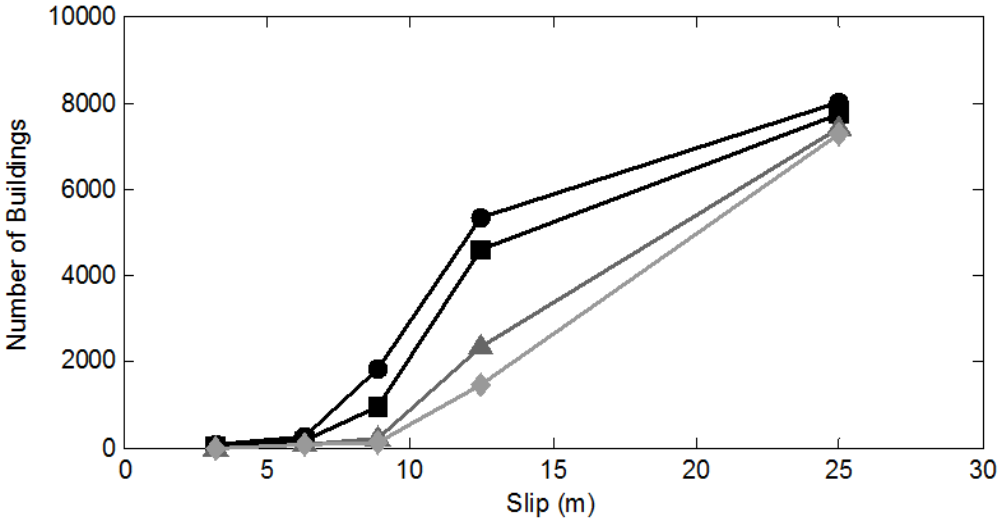

Figure 14 Estimated number of damage buildings for five events and four damage levels for probabilities of occurrence greater than 50%: minor (circle), moderate (square), major (triangle), complete (diamond).

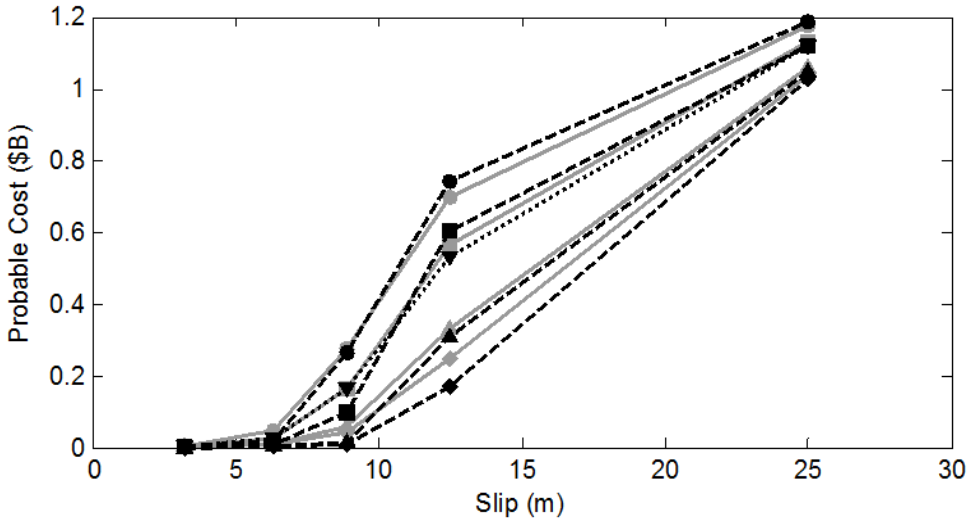

Figure 15 Probable cost (in billions of dollars) for five events and four damage levels for probabilities of occurrence greater than 50%: minor (circle), moderate (square), major (triangle), complete (diamond) damage.

Tables

Table 1 Digital elevation model parameters

	Grid A	**Grid B**	**Grid C**
Lat North (°)	48.00	46.54	46.05
Lat South (°)	44.00	45.65	45.90
Lon North (°)	-123.00	-123.51	-123.89
Lon South (°)	-127.00	-124.40	-124.04
Cellsize (arc sec)	36.00	4.00	1.00
ncols	400	800	538
nrows	400	800	645
Nodes	160,000	640,000	347,010

Table 2 Synthetic tsunami events modeled

Case	M_W	Segment	Length (km)	Width (km)	Slip (m)
1	8.7	acsz–56a to acsz–65b	1000	100	3.15
2	8.9	acsz–56a to acsz–65b	1000	100	6.28
3	9.0	acsz–56a to acsz–65b	1000	100	8.87
4	9.1	acsz–56a to acsz–65b	1000	100	12.53
5	9.3	acsz–56a to acsz–65b	1000	100	25.00

Table 3 Description of various damage levels taken from Suppasri *et al*. (2012)

Damage Level	Description
Minor	window is damaged but no damage on wall
Moderate	window and one part of wall are damaged
Major	window and large part of wall are damaged
Complete	window, wall, and column are damaged

Table 4 Total number of buildings within the inundation zone, total number of buildings with a probability of occurrence greater than 25, 50, and 75% for an estimate of moderate damage, and total number of buildings estimated to have greater the 50% probability of occurrence for minor, moderate, major, and complete damage.

Slip	Total	P Mod. Damage			Number of Buildings P > 50%			
(m)	# Build.	> 25%	> 50%	> 75%	Min.	Mod.	Maj.	Com.
3	908	48	39	0	48	39	0	0
6	4508	233	149	67	234	149	52	48
9	5883	1754	963	448	1819	963	200	132
13	6661	5326	4585	3417	5356	4585	2328	1469
25	8846	8021	7775	7572	8032	7775	7414	7282

Table 5 Probable cost in millions of dollars using methods 1, 2, and 3 for 3, 6, 9, 13, and 25 m of slip.

Slip	Method 1 ($M)				Method 2($M)				Method 3
(m)	Min.	Mod.	Maj.	Com.	Min.	Mod.	Maj.	Com.	($M)
3	3.5	1.9	0.5	0.4	2.4	1.8	0.0	0.0	2.0
6	45.8	23.6	7.9	6.1	16.8	10.4	2.4	2.4	25.8
9	276.7	161.9	57.1	39.7	262.1	97.4	15.2	10.9	165.2
13	697.6	565.5	333.0	249.6	742.4	600.3	308.4	166.9	532.1
25	1176.8	1129.9	1059.2	1033.9	1188.6	1121.7	1046.2	1024.8	1122.0

Table 6 Summary comparison of damage estimates with previous studies

	Wood (2007)	Dominey-Howes *et al.* (2010)	This Study
Hazard	379 Line	500 yr event	3, 6, 9, 13, and 25 m of slip
Assessment	In/Out & Tax Lot Data	PTVA model & Tax Lot Data	Fragility Curves & Tax Lot Data
Assets Inundated ($millions)	843	500	119, 507, 671, 768, and 1324
Estimate Loss ($millions)	-	116	2, 26, 165, 532, and 1122

References

Cercone, C., Naito, C., Riggs, R., & Cox, D. (submitted). Tsunami Generated Debris and Structural Performance Guidelines. *Journal of Waterway, Port, Coastal and Ocean Engineering*.

Cox, D., Tomita, T., Lynett, P., & Holman, R. A. (2008). Kinematics of breaking tsunami wavefronts: a data set from large scale laboratory experiments. *Proc. 31st International Conference on Coastal Engineering* (pp. 1421–1432). ASCE.

Delouis, B., Nocquet, J. M., & Vallée, M. (2010). Slip distribution of the February 27, 2010 Mw = 8.8 Maule Earthquake, central Chile, from static and high-rate GPS, InSAR, and broadband teleseismic data. *Geophysical Research Letters* .

Dominey-Howes, D., Dunbar, P., Varner, J., & Papathoma-Kohle, M. (2010). Estimating probable maximum loss from a Cascadia tsunami. *Natural Hazards*, 43-61.

FEMA P646. (2008). Guidelines for Design of Structures for Vertical Evacuation from Tsunamis. Washington, D.C., USA: Federal Emergency Management Agency.

Gica, E., Spillane, M. C., Titov, V. V., Chamberlin, C. D., & Newman, J. C. (2008). *Development Of The Forecast Propagation Database For NOAA's Short-Term Inundation Forecast For Tsunamis (SIFT): NOAA Technical Memorandum OAR PMEL-139.* Seattle, WA: Pacific Marine Environmental Laboratory.

Geist, E. L. (2005). *Local Tsunami Hazards in the Pacific Northwest from Cascadia Subduction Zone Earthquakes.* U.S. Geological Survey Professional Paper 1661-B .

Goldfinger, C., Nelson, C. H., Morey, A. E., Johnson, J. E., Patton, J. R., Karabanov, E., et al. (2012). *Turbidite Event History—Methods and Implications for Holocene Paleoseismicity of the Cascadia Subduction Zone.* U.S. Geological Survey Professional Paper 1661–F, 170 p.

Gonzalez, F. I., Geist, E. L., Jaffe, B., Kanoglu, U., Mofjeld, H., Synolakis, C. E., et al. (2009). Probabilistic tsunami hazard assessment at Seaside, Oregon, for near- and far-field seismic sources. *Journal of Geophysical Research* , Vol. 114, pp. 1-19.

Hanks, T. C., & Kanamori, H. (1979). A moment magnitude scale. *Journal of Geophysical Research: Solid Earth* , 2348-2350.

Hirata, K., Satake, K., Tanioka, Y., Kuragano, T., Hasegawa, Y., Hayashi, Y., et al. (2006). The 2004 Indian Ocean tsunami: Tsunami source model from satellite altimetry. *Earth Planets Space* , 195-2001.

Ichinose, G., Somerville, P., Thio, H. K., Graves, R., & O'Connell, D. (2007). Rupture process of the 1964 Prince William Sound, Alaska, earthquake from the combined inversion of seismic, tsunami, and geodetic data. *Journal of Geophysical Research* .

Koshimura, S., Oie, T., Yanagisawa, H., & Imanura, F. (2009). Developing Fragility Functions For Tsunami Damage Estimation Using Numerical Model And Post-Tsunami Data From Banda Aceh, Indonesia. *Coastal Engineering Journal* , 243-273.

Murao, O., & Nakazato, H. (2010). Vulnerability Functions For Buildings Based On Damage Survey Data In Sri Lanka After The 2004 Indian Ocean Tsunami. *International Conference on Sustainable Built Environment* , 371-378.

National Tsunami Hazard Mitigation Program. (2012). Proceedings and Results of the 2011 NTHMP Model Benchmarking Workshop. Boulder, CO: Department of Commerce/NOAA/NTHMP; (NOAA Special Report). 436 p.

Okada, Y. (1985). Surface deformation due to shear and tensile faults in a half-space. *Bulletin of the Seismological Society of America* , Vol. 75, No. 4, pp. 1135–1154.

Ozawa, S., Nishimura, N., Suito, H., Kobayashi, T., Tobita, M., & Imakiire, T. (2011). Coseismic and postseismic slip of the 2011 magnitude-9 Tohoku-Oki earthquake. *Nature* , 373-376.

Park, H., Lynett, P. J., Cox, D. T., Wiebe, D. M., & Shin, S. (submitted). Tsunami Inundation Modeling in Constructed Environments: A Physical and Numerical Comparison of Free-Surface Elevation, Velocity, and Momentum Flux. *Coastal Engineering* .

Park, S., van de Lindt, J. W., Cox, D. T., Gupta, R., & Aguiniga, A. (2012). Successive Earthquake-Tsunami Analysis to Develop Collapse Fragilities. *Journal of Earthquake Engineering* , 851-863.

PMEL. *Community Model Interface for Tsunami (ComMIT).* NOAA.

PMEL. (2006). *Method of Splitting Tsunami (MOST) Software Manual.* NOAA.

Priest, G. R. (1995). *Explanation of Mapping Methods and use of the Tsunami Hazard Maps of the Oregon Coast.* Portland, Oregon: Department of Geology and Mineral Industries, Open-File Report O-95-67.

Rueben, M., Holman, R., Cox, D., Shin, S., Killian, J., & Stanley, J. (2011). Optical measurements of tsunami inundation through an urban waterfront modeled in a large-scale laboratory basin. *Coastal Engineering*, 229-238.

Satake, K., Wang, K., & Atwater, B. F. (2003). Fault slip and seismic moment of the 1700 Cascadia earthquake inferred from Japanese tsunami descriptions. *Journal of Geophysical Research* .

Schultz, M. T., Gouldby, B. P., Simm, J. D., & Wibowo, J. L. (2010). *Beyond the Factor of Safety: Developing Fragility Curves to Characterize System Reliability SR-10-1.* U.S. Army Corps of Engineers: Engineering Research and Development Center .

Stern, R. J. (2002). Subduction Zones. *Reviews of Geophysics* .

Suppasri, A., Koshimura, S., & Imamura, F. (2011). Developing tsunami fragility curves based on the satellite remote sensing and the numerical modeling of the 2004 Indian Ocean tsunami in Thailand. *Natural Hazards and Earth System Sciences* , 173-189.

Suppasri, A., Mas, E., Koshimura, S., Imai, K., Harada, K., & Imamura, F. (2012). Developing tsunami fragility curves from the surveyed data of the 2011 Great East Japan tsunami in Sendai and Ishinomaki plains. *Coastal Engineering Journal* .

Suppasri, A., Mas, E., Charvet, I., Gunasekera, R., Imai, K., Fukutani, Y., et al. (2013). Building damage characteristics based on surveyed data and fragility curves of the 2011 Great East Japan tsunami. *Natural Hazards* , 319-341.

Tang, L., Titov, V. V., & Chamberlin, C. D. (2009). Development, testing, and applications of site-specific tsunami inundation models for real-time forecasting. *Journal of Geophysical Research* , Vol. 114, C12.

Titov, V. V., & Synolakis, C. E. (1995). Modeling of breaking and nonbreaking long wave evolution. *Journal of Waterway, Port, Coastal, and Ocean Engineering* , 121(6), 308-316.

Titov, V. V., & Synolakis, C. E. (1998). Numerical modeling of tidal wave runup. *Journal of Waterway, Port, Coastal, and Ocean Engineering* , 124(4), 157–171.

Titov, V. V., Moore, C. W., Greenslade, D. J., Pattiaratchi, C., Badal, R., Synolakis, C. E., et al. (2011). New Tool for Inundation Modeling: Community Modeling Interface for Tsunamis (ComMIT). *Pure and Applied Geophysics* , 168, 2121–2131.

Tsunami Pilot Study Working Group. (2006). *Seaside, Oregon, Tsunami Pilot Study—Modernization of FEMA Flood Hazard Maps.* Joint NOAA/USGS/FEMA Special Report 94.

Wood, N. (2007). *Variations in City Exposure and Sensitivity to Tsunami Hazards in Oregon.* U.S. Geological Survey Scientific Investigations Report 2007-5283 .

Yeh, H. (2006). Maximum Fluid Force in the Tsunami Runup Zone. *Journal of Waterway, Port, Coastal, and Ocean Engineering* , 132, 496-500.

Yeh, H., Robertson, I., & Preuss, J. (2005). Development of Design Guidelines for Structures that Serve as Tsunami Vertical Evacuation Sites. Olympia, WA: *Washington Division of Geology and Earth Resources*: Open File Report 2005-4.

Yoshida, Y., Ueno, H., Muto, D., & Aoki, S. (2011). Source process of the 2011 off the Pacific coast of Tohoku Earthquake with the combination of teleseismic and strong motion data. *Earth Planets Space* , 565-569.

Estimating Hydrodynamic Properties of Tsunami Inundation Using an Energy Method

Dane M. Wiebe

Hyoungsu Park

Daniel T. Cox

David L. Kriebel

American Society of Civil Engineers
Journal of Waterway, Port, Coastal and Ocean Engineering

ASCE Journal Services
1801 Alexander Bell Drive
Reston, VA 20191-4400

To be submitted 2013

Abstract

A new tsunami inundation model based on the concept of an energy grade line was developed to estimate the hydrodynamic quantities of maximum flow depth, velocity, and momentum flux between the shoreline and extent of inundation along a 1D transect. The model allows for either the initial flow depth at the shoreline or the extent of inundation to be specified and is calibrated with a constant Manning's roughness coefficient. The numerical model FUNWAVE was used to develop an empirical relation for the crossshore variation of the Froude number at the time of the maximum momentum flux to separate the relative contribution of the flow depth and velocity to the energy equation. Using averaged coefficients, the model was compared to FUNWAVE simulations for bi-linear slopes ranging from 1:1000 to 1:50 and bottom roughness coefficients ranging from 0.005 to 0.015. The average error for the tuned model in flow depth, velocity, and momentum flux were 10, 23, and 10%, respectively. The model was tested on complex bathymetry without recalibration at Rockaway Beach, Oregon, with errors of 14, 44, and 14% for flow depth, velocity, and momentum flux, respectively.

1.0 Introduction

In recent years tsunamis have gained increasing attention, due to the severity of events such as the 2011 Tohoku tsunami and most notably the 2004 Indian Ocean tsunami. In addition to the catastrophic loss of life, these events can have severe impacts on the constructed environment. The 2011 Tohoku event, for example, damaged 78 bridges, 128,530 houses, and 230,332 buildings (Mori & Takahashi, 2012). Although these events caused widespread damage to structures on a regional scale, design guidance and methods for estimating design loads and damage from future events requires further study.

Some design guidance exists for specialized cases, such as vertical evacuation centers (FEMA P646, 2008; Pimanmas *et al.* 2010), and numerical models exist that can compute the complex details of overland flow (e.g., NTHMP, 2012) including the effects of the constructed environment (e.g., Kaiser *et al.* 2011)). Design engineers lack the methods to determine conservative design loads under realistic tsunami conditions and topographies for hazard assessment on community-wide scale for comparison with loads for other hazards such as earthquake and wind. Yeh (2006) developed an envelope of maximum momentum flux from the runup and rundown processes on a uniformly sloping beach using analytic and numeric forms of the shallow-water theory derived by Carrier *et al.* (2003). Yeh also shows that the analytical solution for bore runup by Shen and Meyer (1963) provides a conservative estimate of the maximum velocity. Both of these solutions will be compared with those presented in this paper.

Several analytical and numerical solutions exist to predict tsunami (solitary wave, N-wave, or longwave) runup on a uniformly sloping beach. The most notable analytical solutions include those of Carrier and Greenspan (1958) who developed an explicit analytical solution for non-linear shallow-water theory, and Synolakis (1987) who derived a theory for runup of non-breaking solitary waves on a plane beach. Over the past decades, tsunamis have primarily been modeled as solitary waves and have

been shown to be in good agreement with numerical and experimental results; however, recent work by Madsen *et al.* (2008) suggests that due to geophysical scale restrictions, the ocean basins are not large enough for tsunamis to progress into solitary waves. Building on Synolakis' work, Madsen and Schaffer (2010) derived a solution, in place of a solitary wave solution, which satisfies the shallow-water equations offshore and the non-linear shallow-water equations onshore for a sloping beach. These methods can be complicated to use and may not be applicable to realistic topographies.

Other research efforts have analyzed wave runup and tsunami inundation from an energy perspective. French (1982) developed a predictive method for wave runup on low bluffs or banks back by a nearly level plateau using the concept of the energy grade line. This method calculates the hypothetical runup elevation on the steeper bluff slope, and uses the energy grade line concept and simple open channel flow equations to determine the runup elevation, and subsequent inundation extent on the milder slope. Cox and Machemehl (1986) focused on defining a safe setback limit and clearance elevation for buildings subject to waves overtopping a berm crest. Their work provided a simplified first approximation of the hydrodynamic conditions from an overtopping wave. The method calculates the incident wave energy, based on the wave height and length, considers the energy dissipation of a bore, and provides an estimate of both the inundation extent, and bore velocity. Similarly, Li and Raichlen (2003) developed a predictive method for estimating wave runup for breaking solitary waves on a plane beach based on the principles of energy conservation. The method balances the incident wave energy with the potential, kinetic, reflected, and dissipated energies. The dissipated energy includes terms for friction at the air water interface, bottom friction, and wave breaking. For the relatively steep slope, 1:15, which the authors where examining, wave breaking dominated the dissipation term, and subsequently the other terms were assumed to be negligible. The model was found to agree reasonably well with small-scale laboratory observations.

The principle of the energy grade line forms the foundation of the method developed in this paper for modeling tsunami inundation. Section 2 presents the methodology of the Energy Grade Line model (EGL). Section 3 introduces the Boussinesq model, FUNWAVE, which was used to model a series of solitary waves on bi-linear beaches to calibrate to EGL model. Section 4 compares the calibrated EGL model to FUNWAVE for the same waves and beaches. Section 5 introduces and compares variations of the EGL model to both the FUNWAVE results and Yeh's equations. Section 6 compares the calibrated EGL model to FUNWAVE on complex bathymetry at Rockaway Beach, Oregon. Finally, Section 7 comments on the model and summarizes key findings.

2.0 Energy Grade Line Methodology

The objective of the EGL model is to provide the maximum values of flow depth, velocity, and momentum flux, along a 1D transect between the shoreline and the extent of inundation for a given maximum flow depth at the shoreline, cross-shore profile, and bottom roughness. Although the tsunami inundation is a non-uniform unsteady flow, with the maximum values of flow depth, velocity, and momentum flux occurring at different times for a given location, the EGL model assumes a non-uniform steady state solution. To achieve this, the model calculates the extent of inundation for a given profile and roughness using the maximum values of flow depth and velocity. Then, the flow depth and velocity at the time of maximum momentum flux are determined by empirical relations based on the maximum flow depth. We note that the importance of the maximum flow depth may be related to the vertical extent of buildings for safe vertical evacuation, the maximum flow speed may be related to the maximum debris impact speed for debris impact loading, and the maximum momentum flux may be related to the base shear force on a building. To avoid confusion, it is mentioned that the maximum flow depth and maximum velocity used to calculate the extent of inundation should not be used to calculate the maximum momentum flux, as it would significantly overestimate that quantity.

For ideal, steady, incompressible fluid flow, the general energy equations maybe be written (Rouse, 1946):

$$\frac{p_1}{\rho g} + \frac{U_1^2}{2g} + z_1 + Sx = \frac{p_2}{\rho g} + \frac{U_2^2}{2g} + z_2 \quad (1)$$

where p is pressure, ρ is fluid density, g is gravity, U is velocity assumed to be depth uniform, z is elevation, and Sx is energy loss, where x is distance from point 1 upstream to point 2 downstream. In open-channel flow, pressure it atmospheric, and constant, so it can be disregarded. If elevation is divided into its two components, flow depth and ground elevation, the general energy equation can be re-written:

$$\frac{U_1^2}{2g} + h_1 + m_1 x + Sx = \frac{U_2^2}{2g} + h_2 + m_2 x \quad (2)$$

where h is the flow depth, and mx is the elevation calculated from the profile slope, m, multiplied by distance, x (Figure 1). The total energy at the shoreline E_o can be related to the available energy at any location between the shoreline by the following relation:

$$E_o = \frac{U^2}{2g} + h + mx + Sx \quad (3)$$

By conservation of energy, E_o is equal to the final (potential) energy at the extent of runup, x_r plus the losses.

$$E_o = (m + S)x_r \quad (4)$$

Starting at the shoreline taken as the datum z = 0, the initial energy is comprised of the flow depth and velocity:

$$E = h + \frac{\mathrm{U}^2}{2g} \quad (5)$$

where the velocity and depth can be related by the Froude number, F_r.

$$F_r = \frac{U}{\sqrt{gh}} \tag{6}$$

Substituting (6) into (5) yields an explicit equation for flow depth based on the available energy for subsequent locations.

$$h = \frac{E}{1 + \frac{F_r{}^2}{2}} \tag{7}$$

The rate of energy loss is taken as the slope of the energy grade line, which is a combination of a change in elevation, mx, and frictional losses calculated by Manning's equation:

$$S = \frac{U^2}{\left(\frac{k}{n}\right)^2 h^{4/3}} \tag{8}$$

where k is a conversion factor (SI k = 1, Imperial units k = 1.46), and n is the Gauckler–Manning coefficient. Recommended values of n for steady flow over floodplains range from 0.020 for cultivated areas to 0.160 for heavily wooded areas (Chow, 1959). NOAA recommends a default value of n = 0.03 for tsunami inundation of bare earth models (PMEL, 2006). Less is known for n for tsunami inundation through constructed environments.

The equations are solved iteratively, where available energy at the next spatial step is determined by the energy loss/gain over the distance between the two steps, Δx:

$$E_{i+1} = E_i + \Delta x \frac{dE}{dx} \tag{9}$$

where the rate of energy loss (or gain) is based on the slope of the energy grade line.

$$\frac{dE}{dx} = m + S \tag{10}$$

Generally, the profile slope is positive, and both the change in elevation and frictional losses will remove energy from the flow. If the profile slope is negative, energy will be transferred back into the flow through an increase in the flow depth and velocity. The total energy available at any subsequent location is given by the following relation.

$$E_{i+1} = \frac{U_1^2}{2g} + h_1 + z_1 + \Delta x(m + S) \tag{11}$$

The EGL model requires the spatial domain to discretized along a single transect, to provide locations at which the equations may be evaluated. The discretization can be uneven, and coarsely spaced; however, the spacing should be close enough to capture dominant geographic features. The flow depth and velocity at each spatial step are a function of F_r, which is a function of the relative extent of inundation x/x_r. Determining the appropriate value of F_r will be discussed further in the next section. Three variations of the energy grade line model were examined and will be discussed in Section 5.

3.0 Tuning with FUNWAVE

FUNWAVE-TVD is used to calibrate the energy grade line model. The model is based the on nonlinear Boussinesq equations, and accounts for wave dispersion, wave breaking, and bottom friction. The numerical scheme is a hybrid of finite volume and finite difference, and runup is modeled using a slot technique. FUNWAVE has been validated to the community accepted benchmarked tests and is in continual use for tsunami inundation studies and hazard mapping funded by the National Tsunami Hazard Mitigation Program (National Tsunami Hazard Mitigation Program, 2012). Further information regarding the theory and numerical implementation of the code is described in Wei & Kirby (1995), Wei *et al.* (1995), Tehranirad *et al.* (2011), Tehranirad *et al.* (2011), and Shi *et al.* (2012; 2011).

Using FUNWAVE, a series of simple bi-linear beaches and solitary waves were modeled to calibrate the EGL model. In total there were 15 cases, comprised of 5 beach slopes, and 3 bottom roughness coefficients. The beach profiles all started at a depth of 300 m with a horizontal bottom, transitioned to an offshore slope of 1:250, and at the shoreline, the slopes transitioned to 1:50, 1:100, 1:250, 1:500, and 1:1000. The bottom roughness coefficients, C_d, were 0.005, 0.010, and 0.015.

Detailed model parameters of FUNWAVE for each case are provided in Table 1. Variation in normalized maximum values of flow depth, velocity, and momentum flux for C_d is shown in Figure 2, and for slope is shown in Figure 3. The momentum flux is defined as $h_M U_M^2$. In all cases the maximum values were observed to be well behaved, and two trends became apparent: (1) maximum values decrease as the bottom roughness coefficient increases, and (2) the maximum values decrease as slope decreases. Intuitively, both of these trends make sense, as more energy is dissipated by friction as the surface becomes rougher and as the length over which the flow travels increases. The variation in flow depth, velocity, and momentum flux for the 15 cases is on the order of 10, 20, and 25%, respectively.

3.1 Bottom Roughness Coefficient

The bottom roughness coefficient is converted to an equivalent Manning's roughness by the following relation:

$$n = \sqrt{\frac{C_d h^{1/3}}{g}} \tag{12}$$

Since the flow depth varies spatially and temporally, the equivalent n also varies both spatially and temporarily. Figure 4 shows the relation between n and h, for the three C_d modeled. With this equation, n increases as both h and C_d increase. For comparison, the equivalent n at the time of maximum momentum flux, M_{max}, was calculated for all 15 cases. For the C_d = 0.005, 0.010, and 0.015 the range of corresponding n for all 5 slopes are 0.013 – 0.027, 0.018 – 0.038, and 0.023 – 0.047,

respectively. The greatest variation of equivalent n values is for the rougher C_d, and milder slopes. The maximum variation was for the case C_d = 0.015 and m = 1:1000 where n varied from 0.017 to 0.047. The range of n modeled in this study are similar to those of Wamsley *et al*. (2010) whom modeled hurricane storm surge over coastal marshes near New Orleans, Lousiana where n values ranged from 0.02 to 0.10. The bottom roughness coefficients for ocean basins are typically taken as C_d = 0.005 (e.g. Zhang *et al.*, 2004). Park *et al.* (submitted) compared numerical and physical model results for the constructed environment of Seaside, Oregon and found that C_d = 0.005 provided the best results using the numerical model COULWAVE (Lynett *et al.*, 2008). Onshore as h decreases the equivalent n decreases and C_d should increase to account for higher roughness, such as vegetation and constructed environments. However, using a roughness coefficient of 0.005 is conservative, as velocities will be higher, and inundation will extend further inland.

3.2 Froude Number

The Froude number, F_r, relates the balance of inertial and gravitational forces and was utilized to partition the energy of the tsunami inundation between h and U at the time of M_{max}. Figure 5 illustrates how F_r at the time of M_{max} varies as a function of the normalized extent of inundation for the beach slope of 1:250.

The initial value of F_r at the shoreline, F_{r_0}, is dependent on C_d (Chanson, 2006) and was found to be less dependent on the slope. For C_d = 0.005, 0.010, and 0.015, the ensemble averages for all the slopes yielded F_{r_0} = 1.55, 1.15, and 0.75, respectively. From the literature, recommended values of F_r for tsunami bore inundation and dam breaks are constant spatially, and range from 0.8 to 3.0 (Bryant, 2008; Lukkunaprasit *et al.* 2009). It is important to note that these reported values correspond to either the initial velocity or the velocity associated with the maximum flow depth, and not at the time of maximum momentum flux.

The discontinuity associated with F_r at the time of M_{max} as seen, for example, at x/x_r = 5.5 in Figure 5C is due to the time in which the maximum values occur. For instance, the time of M_{max} typically occurs between the time of U_{max} and h_{max}. Over this period, at a single location, there are multiple points in time when the combination of flow depth and velocity produce similar values of momentum flux. So, while the value of M_{max} transitions smoothly with inundation extent, the temporal aspect scatters the Froude number, due to the different flow depth and velocity combinations.

Common to all test cases, the F_r decreased linearly with distance. Near the extent of inundation, F_r approached 0.5 for all cases. However, for very mild slopes and rougher bottom friction, a rapid decrease in F_r was evident beyond $x/x_r = 0.9$. The assumption of a minimum F_r of 0.5, is conservative, and prevents the velocity and momentum flux terms from going to zero at the point of maximum inundation.

Using F_r calculated at the time of M_{max} from FUNWAVE, the following linear equation provides an estimate of F_r at any spatial location between the shoreline and extent of inundation:

$$F_r = F_{r_0} + \left(c - F_{r_0}\right)\left(\frac{x}{x_r}\right) \tag{13}$$

where F_{r_0} = 1.5, 1.2, and 0.8 and c = 0.5 for C_d = 0.005, 0.010, and 0.015 respectively, and are relatively insensitive to slope (Table 2). Table 2 provides F_{r_0}, c, and the mean relative absolute error (MRAE) with respect to the predictive equations, where MRAE is computed

$$MRAE = \frac{1}{f_o t}\sum_{i=1}^{t}|e_i| \tag{14}$$

where f_o is the value of the variable of interest at the shoreline, t is the total number of values, and e is the difference between the model prediction (EGL model) and the observed value (FUNWAVE). The MRAE is the mean absolute error (MAE)

normalized by the value at the shoreline. Willmott & Matsuura (2005) recommend using the MAE over other commonly reported error types such as the RMSE as it provides a better comparison of average model-performance and is unambiguous.

We note that other forms other than a linear fit are possible, such as $F_r = F_{r_0}\sqrt{1 - x/x_r}$, but the overall error was higher in this case, so Eq. 12 is adopted for simplicity. It is noted that $F_r = F_{r_0}\sqrt{1 - x/x_r}$ provides a better fit for very mild slopes (m > 1:500) beyond x/x_r = 0.9, as it captures the F_r decay. Evidence of this decay is present in Figure 5C.

3.3 Flow Depth at Time of Maximum Momentum Flux and Maximum Flow Depth

Since the EGL model is tuned based on the maximum momentum flux, the model provides the flow depth at this time as well, h_M. However, engineering design may require the overall maximum flow depth, h_{max}, for example when determining the required building heights for vertical evacuation. Therefore, this subsection shows a simple empirical method to determine h_M, for known h_{max}. Figure 6 shows the ratio of h_M to h_{max} as a function of normalized inundation. Figure 6A shows the variation for a constant slope, m = 1:250, for C_d = 0.005, 0.010, and 0.015; and Figure 6B shows the variation for a constant roughness, C_d = 0.010, for m = 1:50, 1:100, 1:250, 1:500, and 1:1000. For the mildest slopes, 1:250 to 1:1000, the ratio was found to be relatively constant over the extent of inundation and weakly dependent on the roughness. Whereas for the steepest slopes, 1:50 and 1:100, the ratio was found to slightly increase over the extent of inundation. Neglecting this spatial variation, the ensemble average of each slope for all roughness coefficients was calculated, and is shown in Figure 7 as a function of slope.

For the mildest slopes, 1:500 and 1:1000, the flow depth ratio, h_M/h_{max}, asymptote to a maximum value of approximately 0.75. As the slope increases in steepness, $h_M/h_{max}$was found to decrease to a minimum value of 0.45 for the 1:50

slope. For all slopes, the highest bottom roughness coefficient had the highest flow depth ratio. The variation in h_M/h_{max} was quite narrow with an average of approximately 0.02, and a maximum of 0.09. The following equation is based on a power fit of h_M/h_{max} to slope, for all bottom friction coefficients, and provides an estimate of h_M/h_{max} for simple bi-linear beaches:

$$\frac{h_M}{h_{max}} = 0.2m^{0.2} \tag{15}$$

Taking the highest value from this relation, $\frac{h_M}{h_{max}} \sim 0.75$, provides the upper bound of the envelope for h_M.

4.0 Comparison of the Energy Grade Line Model to FUNWAVE for Idealized bi-linear Beaches

Combining equations (3), (6), (7), (8), and (11) together with equations (13) and (15) the values $h(x)$, $U(x)$, $M(x)$, can be estimated given a cross-shore profile, h_0, F_{r_0}, and n. Figure 8 compares the cross-shore variation of h, U, and M between the FUNWAVE Case 13, C_d = 0.015 and m = 1:250, and the EGL model using n = 0.020 and the average coefficients of F_{r_0} and c in Table 2. All three quantities, $h(x)$, $U(x)$, $M(x)$, are accurately estimated with maximum mean absolute error (MAE) of 0.5 m, 1.1 m/s, and 10.2 m^3/s^2, respectively. The accuracy of U_{max} could be improved if U_{max} and h_{max} were used to calculate F_r instead of the conditions at the time of maximum momentum flux, U_M and h_M. Using F_r at the time of M_{max} provides a conservative estimate of U_{max}. The extent of inundation from FUNWAVE is 1150 m, whereas in the EGL model it is 975 m, approximate 85% of the FUNWAVE value. The extent of inundation from the energy grade line model could match the FUNWAVE results if a lower estimate of n was given.

Figure 9 compares the MRAE of the estimate of h_{max}, U_{max}, and M_{max} for n = 0.010, 0.020, and 0.030 for C_d = 0.010. The average MRAE of h_{max}, U_{max}, and M_{max} over all slopes, C_d, and n are approximately 14, 28, and 13%, respectively, with

maximums of 36, 66 and 42%, respectively. The highest errors for flow depth and momentum flux occur for the mildest slopes, where the extent of inundation and the energy dissipated due to friction are greatest. For steeper slopes, the model is less sensitive to the choice of n, as the change in elevation dominates energy loss. For velocity, the highest error occurred for the steepest slopes, which is due to using F_r at the time of M_{max}. As shown in Figure 7, h_M/h_{max} decreases from 0.75 for 1:1000 to 0.45 for 1:50. Therefore, using F_r at the time of M_{max} increases the error in U_{max} for steeper slopes. In any case, Figure 9 shows that momentum flux can be predicted with an accuracy of approximately 10% to 20% over a range of slopes and relatively insensitive to n.

Figure 10 shows the optimum choice of n with respect to the minimum MRAE of momentum flux. For the milder slopes, 1:100 to 1:1000, the optimum choice of n is approximately 0.020. For the steepest slope, 1:50, the optimum n is significantly higher (rougher), with an average of 0.035. This is most likely attributed to the difference in energy dissipation, and the increase in equivalent bottom roughness for shallow flow depths.

This section highlighted the importance of choosing an appropriate value of n, and the sensitivity of the modeled quantities of $h(x)$, $U(x)$, $M(x)$, and extent of inundation to that choice of n, compared to the FUNWAVE results. For slopes ranging from 1:100 to 1:1000, the model is relatively robust; however, for the steepest slope modeled, 1:50, the model required higher estimates of roughness to achieve similar results to FUNWAVE.

5.0 Variants of the Energy Grade Line Model and Comparison with Other Methods

Two variations of the EGL model were developed and evaluated. The first variant (Method B) is similar to that presented in the methodology section. However, instead of specifying n and allowing x_r to vary, n is varied to match a given x_r. The second variant (Method C) was also developed to match a given extent of inundation,

x_r. In this case however, n is specified and E_0 is varied to match x_r. The flow depth and velocity are still determined by equations (6) and (7) and the bottom slope m is assumed known. Table 3 provides a summary of the required input parameters, free variables, and output from the three variations of the energy grade line model.

The accuracy of the EGL model variations are evaluated against the equations developed by Shen and Meyer (1963) for U_{max} and Yeh (2006) for M_{max}. The maximum velocity is given by the following equation (Shen & Meyer, 1963):

$$U = \sqrt{2gmx} \tag{16}$$

The relation is similar to equation (6) which is used in the EGL model; where $\sqrt{2}$ is an estimate of F_r, and mx the runup elevation, is similar to the flow depth.

The envelope curve of M_{max} is given by the following relations (Yeh, 2006)

$$M = gm^2{x_r}^2\left[0.11\left(\frac{x}{x_r}\right)^2 + 0.015\left(\frac{x}{x_r}\right)\right] \tag{17}$$

Methods A, B, and C of the EGL model, the equations of Shen and Meyer, and Yeh, were evaluated and compared to the FUNWAVE results for all 15 cases. For all the EGL models, F_{r_0} was again taken as 0.8, 1.2, and 1.5 for C_d = 0.005, 0.010, and 0.015, respectively. For methods A and C, n was taken as 0.020.

Figure 11, 12, and 13 show the comparison between the three methods and Case 8 (m = 1:250, C_d = 0.010) for h_{max}, U_{max}, and M_{max} respectively. For clarity, the maximum values of h, U, and M, which occur at the shoreline, are plotted near the upper right hand corners of these figures.

The maximum flow depths for method A are underestimated due to the choice of n. For this case, n = 0.015 was to rough, which lead to an underestimate of x_r, as shown by the modeled value of 0.0 m for a FUNWAVE value of 1.0 m (Figure 11). For both methods B and C, h_{max} is accurately estimated and is conservative.

For maximum velocity, equation (16) of Shen and Meyer provides a conservative upper bound on the maximum value (at the shoreline), which is in agreement with Yeh (Figure 12). Over the extent of inundation, however, the value decreases below the FUNWAVE value (Figure 12). For the EGL models, the trends are similar to those observed for h_{max}. Both method B and C provide accurate and conservative estimates. Method A also provides an accurate estimate near the shoreline, but again underestimates values due to the difference in x_r.

For maximum momentum flux, Method A, B, and C all provide accurate, conservative estimates (Figure 13). Unlike h_{max}, and U_{max} estimates, the underestimate of M_{max} by Method A near the extent of inundation is barely evident. This is due to the rapid decrease in momentum flux with distance from the shoreline.

The accuracy of the estimate of M_{max} by Yeh's equation is found vary significant with slope. For steep slopes, 1:50, the equation is found to accurately estimate the maximum value which occurs at the shoreline. For mild slope, 1:250 and less, the equation severely underestimates the maximum value. In equation (17), the M_{max} scales with $m^2{x_r}^2$. This implies that for very mild beaches, the x_r must be large, or else the M_{max}will be small. For example, to match Case 8 where m = 1:250, M = 80 m^3/s^2, and x_r= 1300 m, the extent of inundation would need to have been approximately 2000 m, 1.5 times the quantity modeled by FUNWAVE. However, the accuracy of Yeh's equation increases for steeper slopes, and it may be more appropriate for slopes of 1:50 and steeper, which is beyond what was analyzed. Figure 14 shows the $M_{0_{FUN}}/M_{0_{Yeh}}$as a function of m at the shoreline where $M_{0_{Yeh}} = 0.125gm^2{x_r}^2$. A polynomial was fit to the data and provides a scaling coefficient to correct Yeh's equation for mild slopes. While this equation improves the estimates, it was not used in the comparison analysis.

$$M_{0_{FUN}}/M_{0_{Yeh}} = 6E^{-6}m^2 + 6E^{-3}\text{m} + 0.7 \quad (18)$$

Details of the M_{max} comparison between the various methods and FUNWAVE for the 15 cases and n = 0.020 are listed in Table 4. The table provides the MRAE over the entire extent of inundations, as well as the maximum and minimum values of AE at any one location. The table identifies the accuracy and sensitivity of each method with respect to m and C_d. Methods A and C each had the minimum MRAE for 7 of the 15 cases, and method B had 1 case. The maximum AE was equally distributed between methods A, B, and Yeh. The minimum AE was predominantly for the Yeh model, with 13 of 15 cases, indicated that the model significantly under predicted the results for mild slopes.

Table 5 provides the average and maximum values of the MRAE, maximum AE, and minimum AE in momentum flux of the 15 cases, for the three n values. The table condenses the information provided in Table 4, from 15 cases to a single value, and lists the accuracy and sensitivity of the methods to the choice of n. The maximum and average values listed in the bottom of Table 4 correspond to n = 0.020 listed in Table 5. Table 6 and Table 7 list the same information as contained with Table 5, but for maximum flow depth, and maximum velocity. From the information listed in Tables 4 to 7, it can be gained that the simplified energy methods provide accurate, conservative estimates of flow depth, velocity, and momentum flux over a range of slopes and bottom roughness.

6.0 Application of the EGL Model to a Realistic Coastal Transect

To evaluate the potential use of the EGL model for a realistic section of coastline, a comparison between the EGL model without recalibration and FUNWAVE was performed for a 1D transect at Rockaway Beach, Oregon. Bathymetric and topographic data was obtained from high-resolution digital elevation model for Garibaldi, Oregon (gov.noaa.ngdc.mgg.dem:249) provided by the National Oceanic and Atmospheric Administration and National Geophysical Data Center. The Garibaldi DEM is referenced to MHW, with a spatial resolution of 1/3 arc-second, approximately 10 m. The modeled transect extended 70 km offshore, with detailed

bathymetric data available for the first 50 km, after which the a liner 1:250 slope extended to a horizontal bottom at a depth of 300 m. Onshore, the transect extended 4 km with a maximum elevation of 375 m. The transect spacing was 25 m, which was high enough resolution to capture details of dominant bathymetric and topographic features (Figure 15). The offshore and onshore slopes are approximately 1:250 and 1:70, respectively. After approximately x = 550 m, the onshore slope increases to 1:15 at the base of a small coastal mountain.

The Rockaway Beach transect was modeled with FUNWAVE using a C_d = 0.005 for an offshore solitary waves condition measuring 2.5 m at a depth of 300 m. The EGL model was run using F_{r_0} = 1.5, c = 1.0, and n = 0.020 (Figure 16).

The MRAE for h, U, and M was 14, 44, and 14%, respectively. For relatively steep slopes, the model is not overly sensitive to the choice of n, as the change increase in elevation dominants the energy loss. For this example, 69% of the total energy loss was due to an increase in elevation, whereas only 31% was dissipated as friction. For this example it was found that n ranging from 0.005 to 0.025 provided similar results.

7.0 Conclusion

A new tsunami inundation model based on the concept of an energy grade line was developed to estimate the hydrodynamic quantities of maximum flow depth, velocity, and momentum flux between the shoreline and extent of inundation along a 1D transect. The model allows for either the initial flow depth at the shoreline or the extent of inundation to be specified and is calibrated with a constant Manning's roughness coefficient. An empirical relation for the crossshore variation of the Froude number at the time of the maximum momentum flux is used to separate the relative contribution of the flow depth and velocity to the energy equation. Primary conclusions are:

1. The F_r at the time of M_{max} was shown to vary spatially. A relation was developed as a function of x/x_r and was shown be relatively insensitive to slope in the range 1:1000 to 1:50.
2. A strong correlation between h_M/h_{max} and m was found with values ranging from 0.45 to 0.75. The value of h_M/h_{max} was also found to be relatively constant over x.
3. The EGL model provides a robust estimate of $h(x)$, $U(x)$, and $M(x)$ for a range of simple bi-linear beaches and bottom roughness coefficients. For n = 0.020, the average MRAE over all 15 cases for h_{max}, U_{max}, and M_{max} were 10, 23, and 10%, respectively.
4. The EGL model methods B and C provide an accurate estimate of $h(x)$, $U(x)$, and $M(x)$ when only given x_r. For n = 0.020, the average MRAE over all 15 cases for both methods B and C for h_{max}, U_{max}, and M_{max} were 10, 14, and 7%, and 12, 9, and 14%, respectively.
5. The EGL model was shown to provide an accurate estimate of $h(x)$, $U(x)$, and $M(x)$ for complex bathymetry at Rockaway Beach, Oregon.

Suggested future work could include validation of offshore roughness coefficients used in numerical models. Common benchmark test only measure a models accuracy of the free surface; however, the choice in roughness has a large influence on velocity and momentum flux, which may be better predictors of damage.

Acknowledgements

This work was funded by the Oregon Sea Grant. The authors thank Gary Chock and Ian Robertson for their constructive comments during the development of the model.

Figures

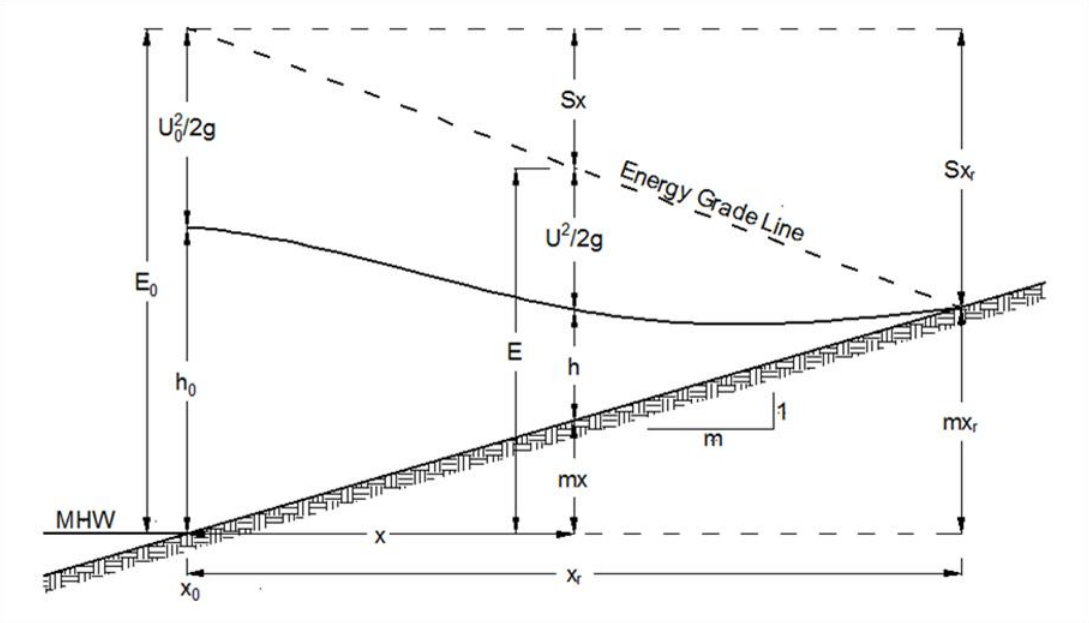

Figure 1: Definition sketch for the energy grade line model.

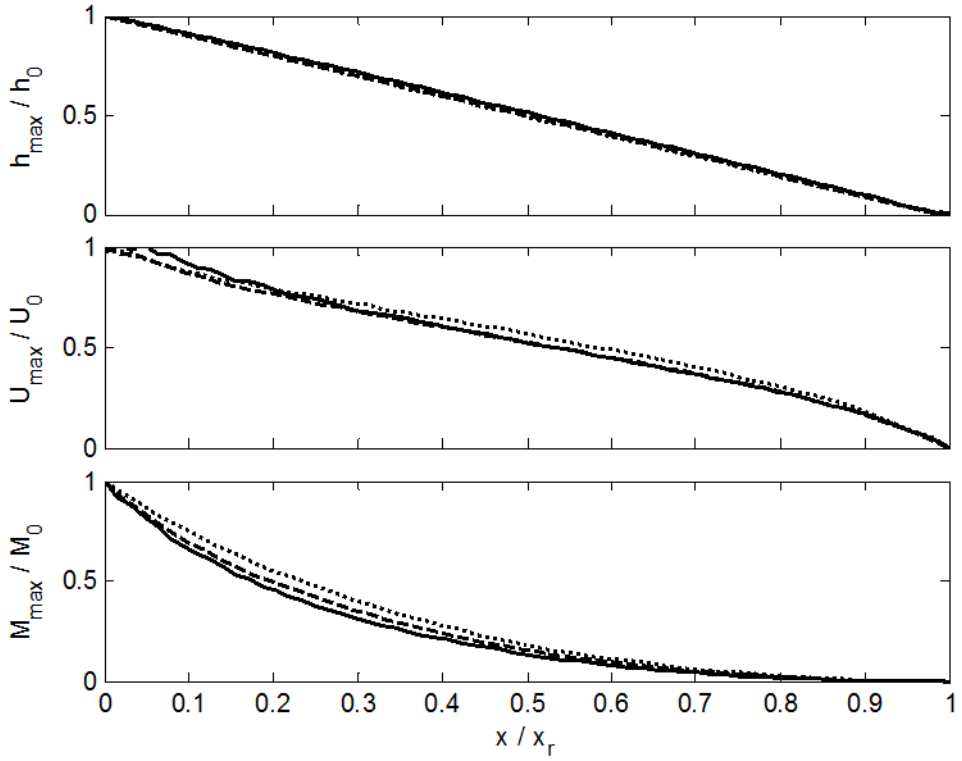

Figure 2: Normalized maximum values of flow depth, velocity, and momentum flux for m = 1:250 and C_d= 0.005 (dotted), 0.010 (dashed), 0.015 (solid) (Cases 3, 8, and 13).

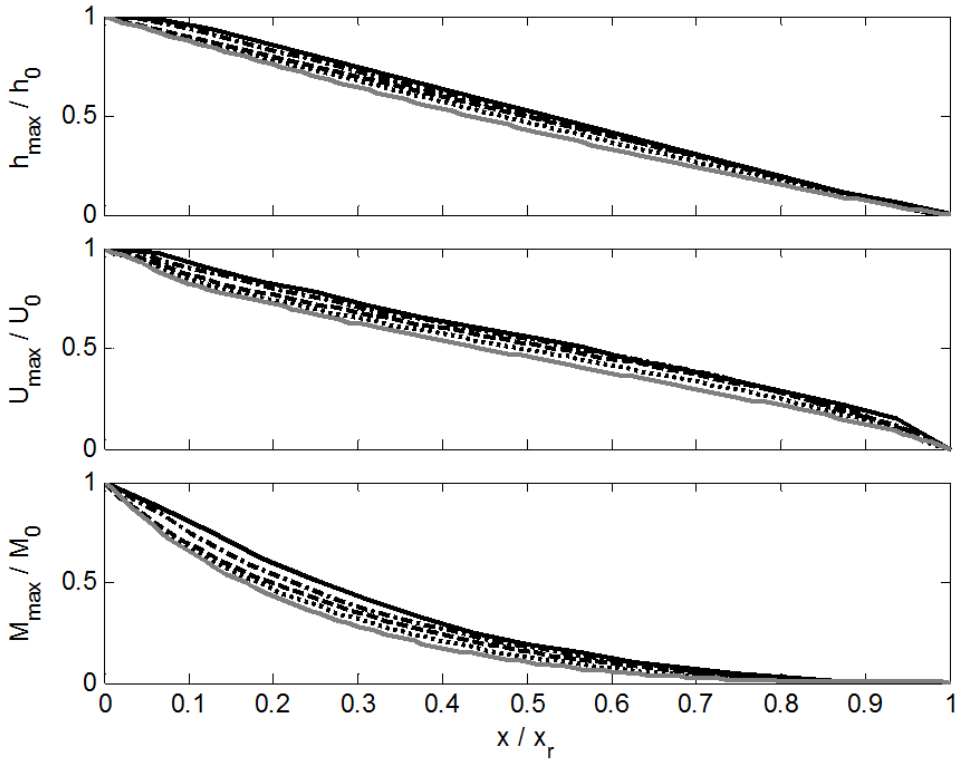

Figure 3: Normalized maximum values of flow depth, velocity, and momentum flux for C_d= 0.010 and m = 1:50 (solid), 1:100 (dashed-dotted), 1:250 (dashed), 1:500 (dotted), and 1:1000 (solid gray) (Cases 6, 7, 8, 9, and 10).

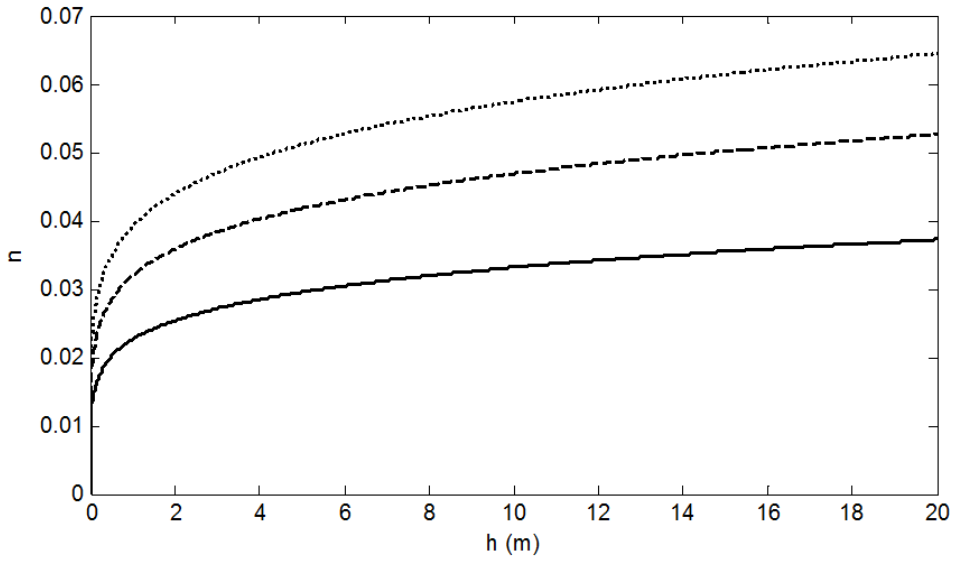

Figure 4: Equivalent n at various flow depths for C_d = 0.005 (solid), 0.010 (dashed), and 0.015 (dotted)

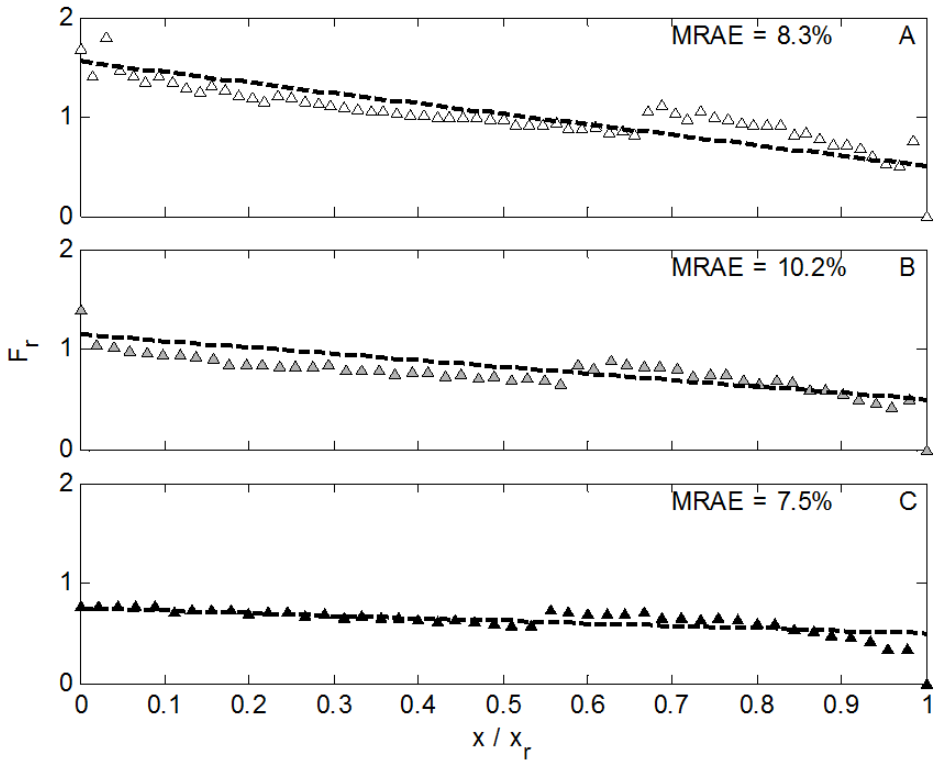

Figure 5: F_r as a function of normalized inundation x/x_r for m = 1:250 and C_d = 0.005 (a), 0.010 (b), and 0.015 (c) computed from FUNWAVE at the time of maximum momentum flux (black circles), and line predictive equation (black dashed line).

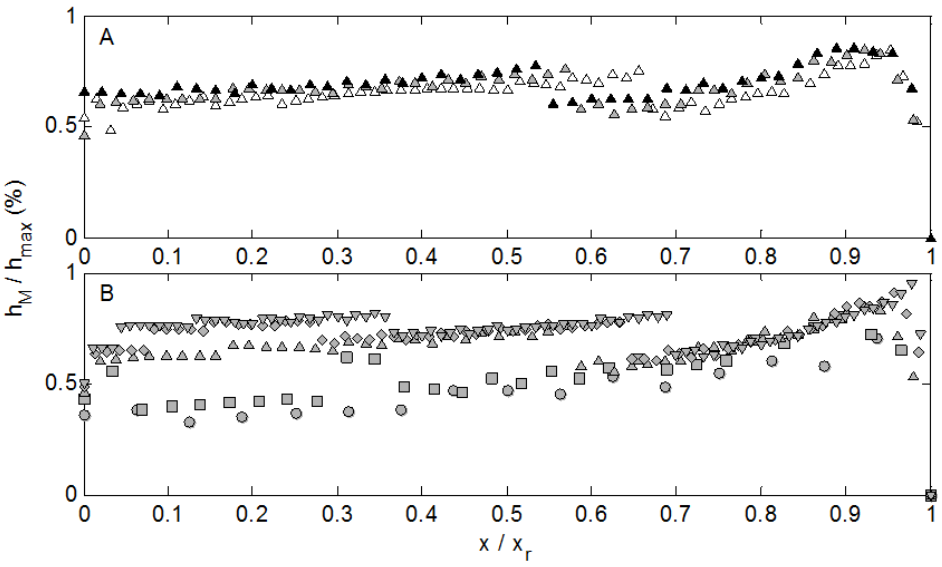

Figure 6: Ratio of flow depth at maximum momentum flux to maximum flow depth as a function of normalized inundation. (A) m = 1:250 for C_d = 0.005 (white), 0.010 (gray), and 0.015 (black). (B) C_d = 0.010 for m = 1:50 (circle), 1:100 (square), 1:250 (triangle), 1:500 (diamond), 1:1000 (inverted triangle).

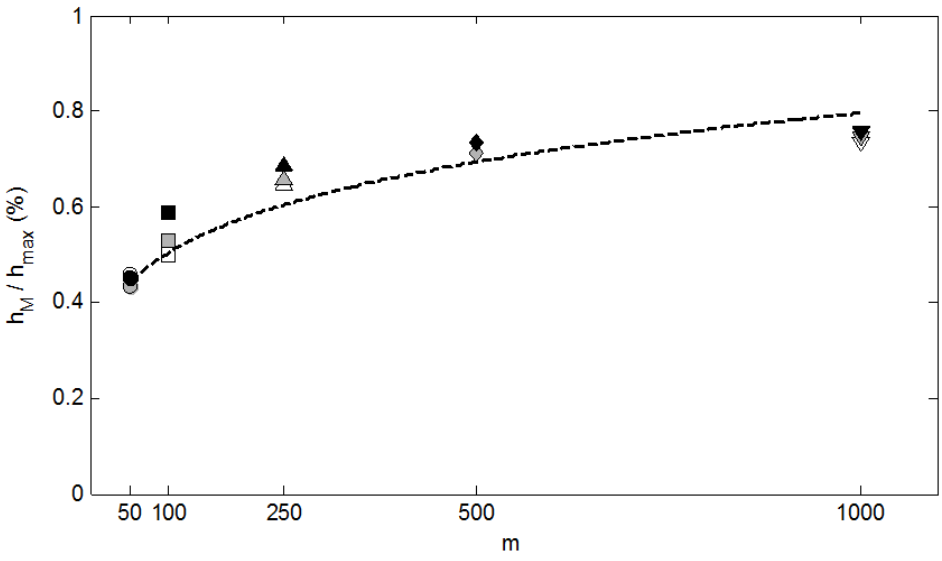

Figure 7: h_M/h_{max} as a function of slope. C_d = 0.005 (white), 0.010 (gray), and 0.015 (black), $m =$ 1:50 (circle), 1:100 (square), 1:250 (triangle), 1:500 (diamond), 1:1000 (inverted triangle), and power fit (black dashed line).

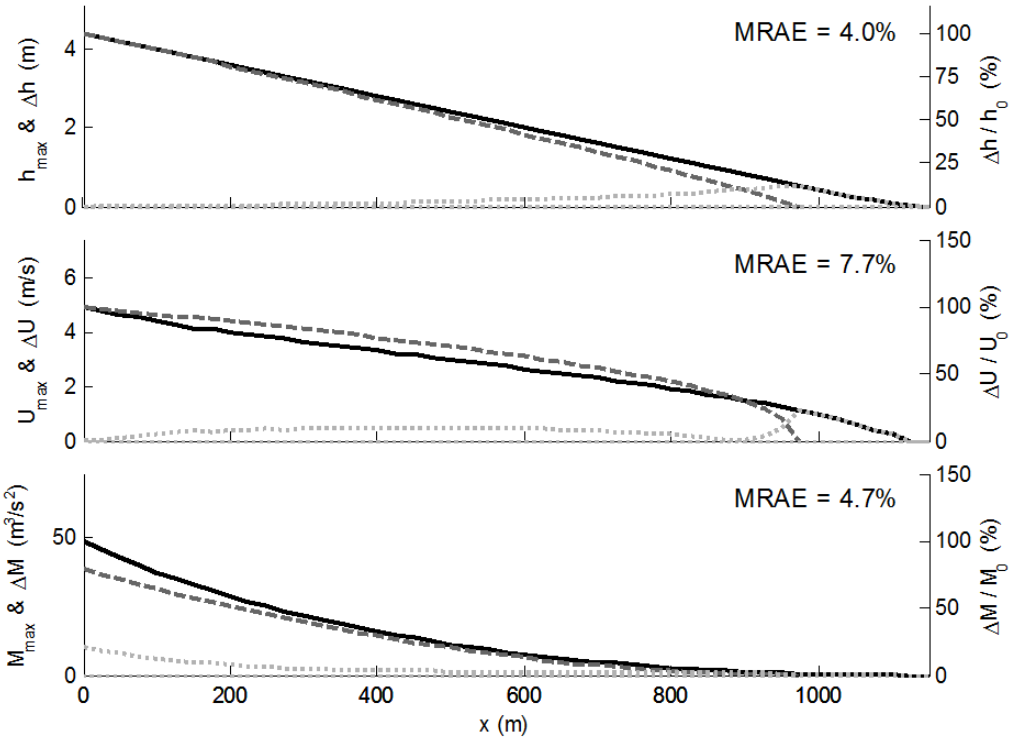

Figure 8: EGL model and FUNWAVE comparison for C_d = 0.015 and m = 1:250. FUNWAVE (solid), EGL Model with n = 0.020 (dashed), and error (dotted).

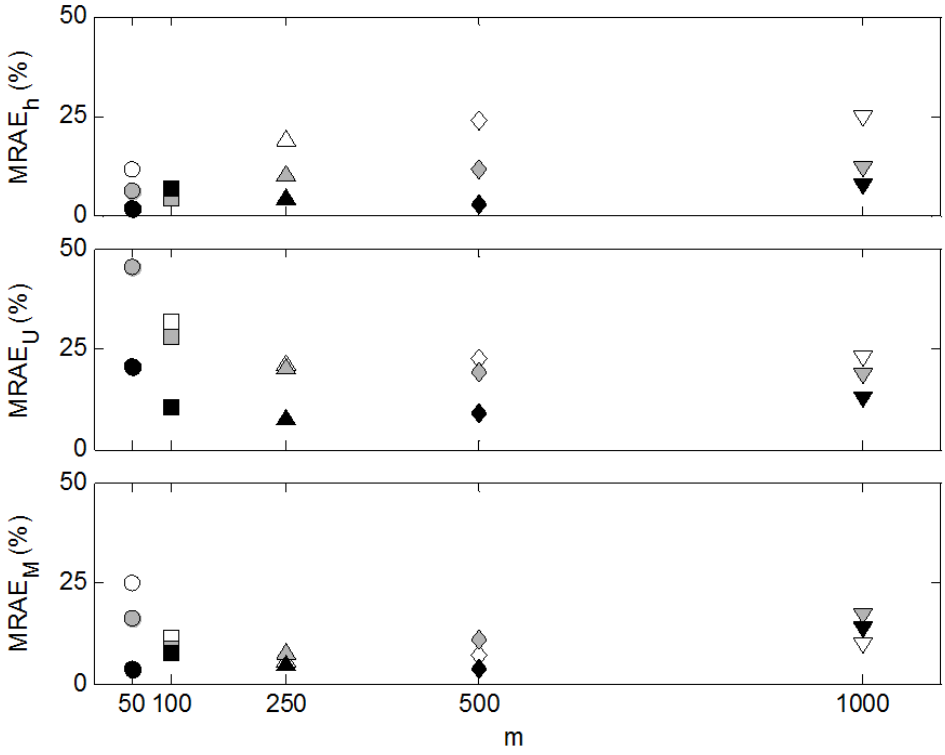

Figure 9: Mean relative absolute error for n = 0.010 (white), 0.020 (gray), and 0.030 (black), for m = 1:50 (circle), 1:100 (square), 1:250 (triange), 1:500 (diamond), and 1:1000 (inverted triangle), for C_d = 0.010. Note the black triangle corresponds to the MRAE computed for Figure 8.

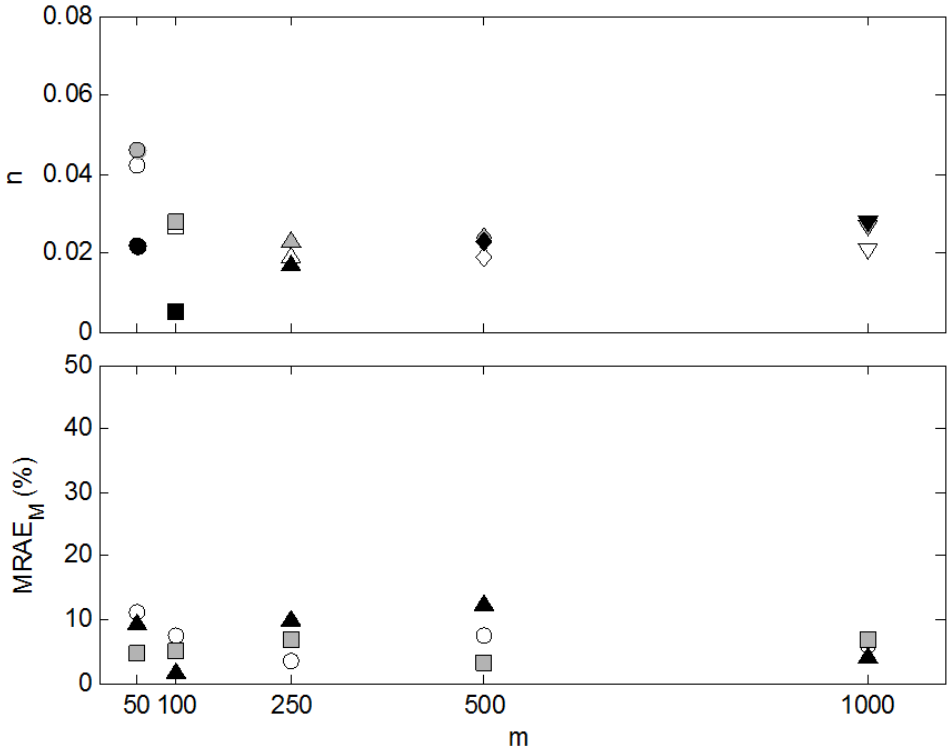

Figure10: Manning's n corresponding to the minimum value of error in momentum flux for C_d = 0.005 (white), 0.010 (gray), and 0.015 (black), for m = 1:50 (circle), 1:100 (square), 1:250 (triange), 1:500 (diamond), and 1:1000 (inverted triangle).

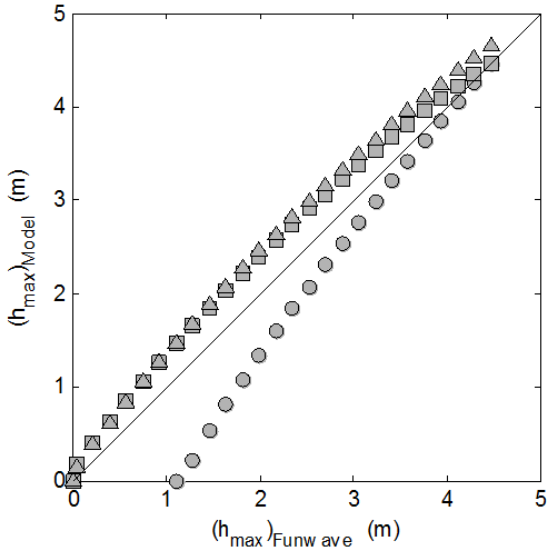

Figure 11: Comparison of maximum flow depth for Case 8 (m = 1:250, C_d = 0.010) and n = 0.020; EGL1 (circle), EGL2 (square), and EGL3 (triangle).

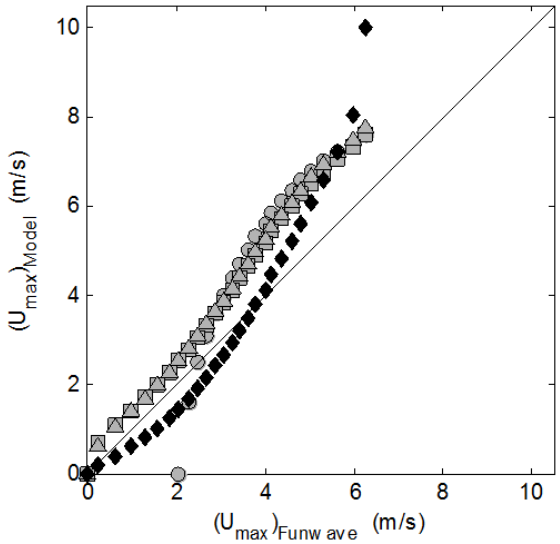

Figure 12: Comparison of maximum velocity for Case 8 (m = 1:250, Cd = 0.010) and n =0.015. EGL1 (circle), EGL2 (square), EGL3 (triangle), and Shen and Meyer (diamond).

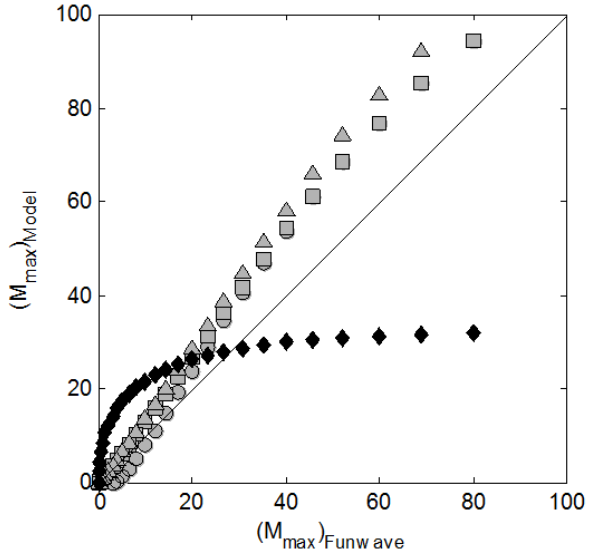

Figure 13: Comparison of maximum momentum flux for Case 8 (m = 1:250, Cd = 0.010) and n =0.015. EGL1 (circle), EGL2 (square), EGL3 (triangle), and Yeh (diamond).

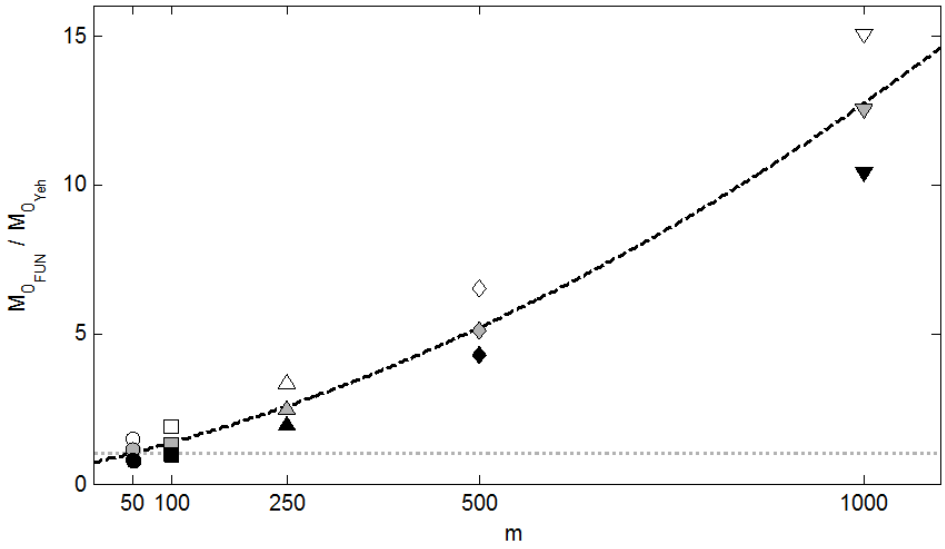

Figure 14: Comparison of $M_{0_{FUN}}/M_{0_{Yeh}}$ as a function of m for all 15 cases. C_d = 0.005 (white), 0.010 (gray), and 0.015 (black), for m = 1:50 (circle), 1:100 (square), 1:250 (triange), 1:500 (diamond), and 1:1000 (inverted triangle), a polynomial of best fit (dashed) and line of unity (dotted).

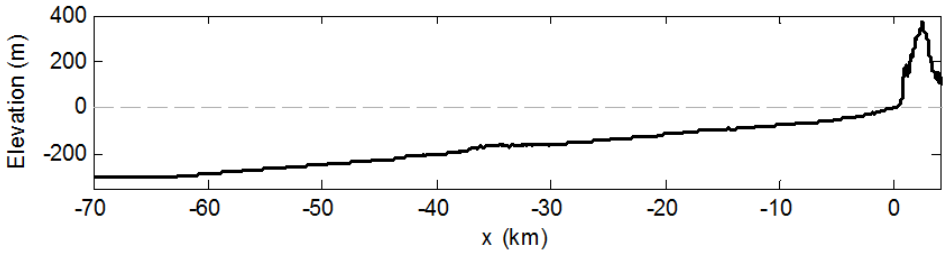

Figure 15: Rockaway Beach Bathymetry where $z = 0$ corresponds to MHW and $x = 0$ is the shoreline corresponding to the intersection of the bathymetry with MHW.

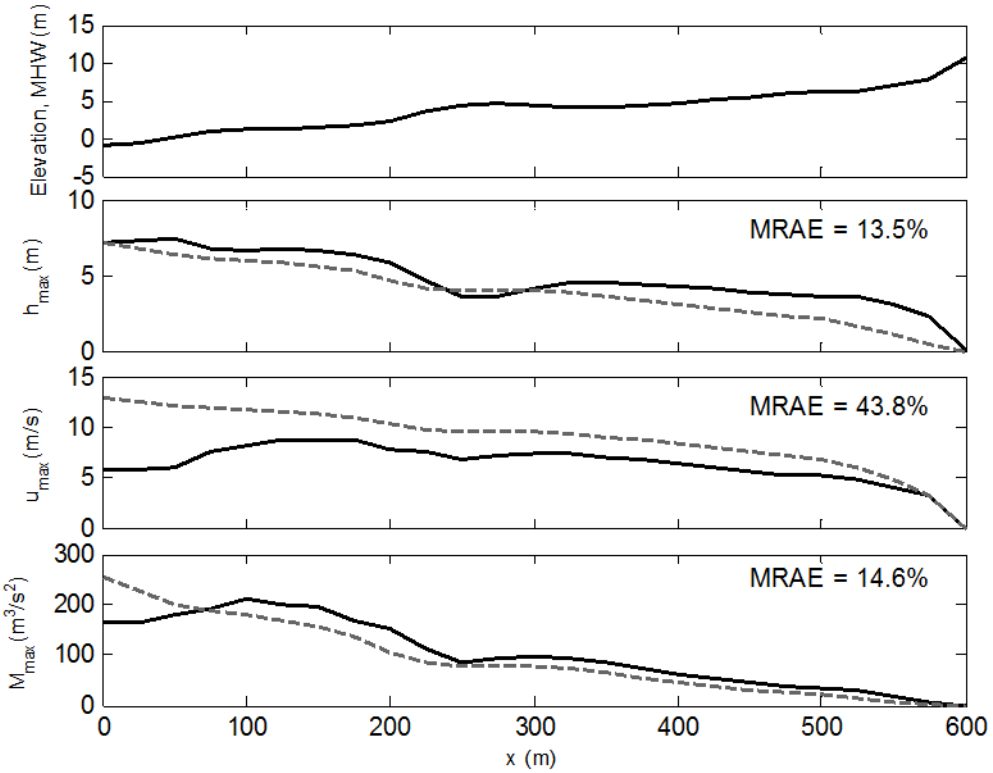

Figure 16: EGL model and FUNWAVE comparison for Rockaway Beach, OR. EGL (dashed) and FUNWAVE (solid).

Tables

Table 1: Summary of FUNWAVE simulations.

Case	C_D	m	h_0 (m)	U_0 (m/s)	M_0 (m^3/s^2)	F_{R_0}	x_r (m)
1	0.005	1:50	6.51	7.58	134.65	1.46	450
2	0.010	1:50	6.36	6.27	81.76	1.19	400
3	0.015	1:50	5.95	4.96	47.40	0.89	375
4	0.005	1:100	5.25	7.58	133.81	1.63	775
5	0.010	1:100	5.34	6.28	81.49	1.21	725
6	0.015	1:100	5.10	4.98	49.05	0.71	650
7	0.005	1:250	4.58	8.38	168.37	1.55	1600
8	0.010	1:250	4.47	6.26	80.17	1.08	1275
9	0.015	1:250	4.38	4.94	48.76	0.77	1125
10	0.005	1:500	4.19	8.35	167.36	1.57	2275
11	0.010	1:500	4.17	6.27	79.90	1.11	1775
12	0.015	1:500	4.13	4.96	49.59	0.71	1525
13	0.005	1:1000	4.06	8.33	166.86	1.59	2975
14	0.010	1:1000	4.03	6.28	79.75	1.10	2250
15	0.015	1:1000	4.00	4.97	50.25	0.73	1950

Table 2: F_{r_0}, c, and MRAE for the 15 modeled cases

	C_D	1:50	1:100	1:250	1:500	1:1000	Average	Modeled
F_{r_0}	0.005	1.46	1.63	1.55	1.57	1.59	1.56	1.5
	0.010	1.19	1.21	1.08	1.11	1.10	1.14	1.2
	0.015	0.89	0.71	0.77	0.71	0.73	0.76	0.8
c	0.005	0.54	0.55	0.61	0.56	0.50	0.55	0.5
	0.010	0.36	0.43	0.50	0.48	0.44	0.44	0.5
	0.015	0.30	0.44	0.45	0.46	0.40	0.41	0.5
MRAE	0.005	8.03	10.93	8.29	9.54	10.12	9.38	-
(%)	0.010	8.40	9.41	10.15	11.35	12.25	10.31	-
	0.015	15.24	11.58	7.55	7.45	7.89	9.94	-

Table 3: Variations of energy grade line model

EGL Model	Input	Free Variables	Output
Method A	h_0, n, m, F_{R_0}	x_r	$h(x), U(x), M(x)$
Method B	h_0, x_r, m, F_{R_0}	n	$h(x), U(x), M(x)$
Method C	n, x_r, m, F_{R_0}	E_0	$h(x), U(x), M(x)$

Table 4: Error in momentum flux for n = 0.020

	MRAE				AE_{max}				AE_{min}			
Case	EGLA	EGLB	EGLC	Yeh	EGLA	EGLB	EGLC	Yeh	EGLA	EGLB	EGLC	Yeh
1	25.0	11.4	7.9	19.8	62.3	60.3	0.0	41.6	0.4	0.0	-34.3	-44.2
2	11.2	7.8	1.4	16.9	35.0	33.0	5.0	30.0	-1.4	-0.4	-9.0	-62.9
3	5.4	6.8	13.8	14.0	18.7	28.6	62.7	18.6	-17.6	0.0	0.0	-118.1
4	7.3	11.8	27.9	14.8	33.3	47.1	145.3	7.9	-25.4	0.1	0.0	-141.7
5	9.9	21.0	49.3	15.9	77.1	88.3	283.4	2.8	-28.5	0.4	0.0	-155.8
6	16.1	7.2	4.6	27.3	23.5	20.7	0.0	37.0	0.0	0.0	-12.9	-11.2
7	8.3	6.0	4.4	24.1	15.5	12.5	9.4	31.0	-0.7	0.0	0.0	-19.6
8	7.5	8.0	10.4	14.5	17.2	17.0	23.6	12.6	-3.8	0.0	0.0	-48.3
9	10.9	13.8	17.5	15.6	28.3	28.8	41.2	4.9	-4.5	0.0	0.0	-64.3
10	17.0	23.9	27.8	17.9	52.9	53.4	70.5	1.6	-4.6	0.1	0.0	-73.4
11	3.5	4.7	3.6	54.0	0.5	0.2	0.3	38.0	-9.2	-9.2	-7.6	7.0
12	7.5	7.5	2.1	35.4	0.0	0.0	0.1	26.6	-12.4	-12.5	-4.5	0.4
13	4.7	4.6	2.4	15.8	0.0	0.1	0.1	10.1	-10.2	-10.2	-6.3	-23.9
14	3.8	2.4	3.0	16.6	3.6	1.5	0.6	3.5	-4.6	-4.6	-8.8	-38.0
15	13.9	9.0	3.9	19.2	12.5	8.1	3.0	1.3	0.0	0.0	-6.5	-45.4
Avg.	10.1	9.7	12.0	21.5	25.4	26.6	43.0	17.8	-8.2	-2.4	-6.0	-56.7
Max.	25.0	23.9	49.3	54.0	77.1	88.3	283.4	41.6	-28.5	-12.5	-34.3	-155.8

Table 5: Summary of error in momentum flux for all case

		MRAE				AE_{max}				AE_{min}			
	n	EGL1	EGL2	EGL3	Yeh	EGL1	EGL2	EGL3	Yeh	EGL1	EGL2	EGL3	Yeh
Avg.	0.010	19.4	9.7	7.6	21.4	37.9	26.6	0.3	17.8	-2.4	-2.4	-34.7	-56.0
	0.020	10.1	9.7	12.0	21.4	25.4	26.6	43.0	17.8	-8.2	-2.4	-6.0	-56.0
	0.030	10.1	9.7	43.0	21.4	22.8	26.6	191.8	17.8	-21.4	-2.4	-0.6	-56.0
Max.	0.010	42.3	23.9	14.9	54.0	113.2	88.3	3.5	41.6	-12.5	-12.5	-65.1	-155.8
	0.020	25.0	23.9	49.3	54.0	77.1	88.3	283.4	41.6	-28.5	-12.5	-34.3	-155.8
	0.030	18.1	23.9	170.5	54.0	74.2	88.3	1110.9	41.6	-70.7	-12.5	-6.5	-155.8

Table 6: Summary of error in flow depth for all case

		MRAE				AE_{max}				AE_{min}			
	n	EGL1	EGL2	EGL3	-	EGL1	EGL2	EGL3	-	EGL1	EGL2	EGL3	-
Avg.	0.010	13.0	7.0	8.5	-	1.1	0.5	0.1	-	0.0	0.0	-1.2	-
	0.020	9.9	7.0	9.4	-	0.2	0.5	0.5	-	-0.3	0.0	-0.7	-
	0.030	19.2	7.0	26.9	-	0.0	0.5	1.9	-	-0.9	0.0	-0.3	-
Max/Min	0.010	28.4	13.1	16.5	-	2.3	1.0	0.4	-	-0.2	-0.1	-2.3	-
	0.020	24.8	13.1	26.4	-	1.4	1.0	1.5	-	-1.3	-0.1	-2.1	-
	0.030	36.3	13.1	72.9	-	0.2	1.0	5.2	-	-2.3	-0.1	-1.8	-

Table 7: Summary of error in velocity for all case

		MRAE				AE_{max}				AE_{min}			
	n	EGL1	EGL2	EGL3	S&M	EGL1	EGL2	EGL3	S&M	EGL1	EGL2	EGL3	S&M
Avg.	0.010	36.3	14.3	7.9	14.0	3.3	1.8	0.9	3.6	0.7	0.2	-0.3	-0.7
	0.020	23.3	14.3	13.9	14.0	1.9	1.8	1.7	3.6	-1.4	0.2	0.0	-0.7
	0.030	25.5	14.3	23.5	14.0	1.6	1.8	2.9	3.6	-3.0	0.2	0.1	-0.7
Max/Min	0.010	66.2	25.9	15.3	32.3	7.1	4.8	2.4	6.8	-0.3	-0.3	-1.5	-2.2
	0.020	58.8	25.9	21.9	32.3	5.4	4.8	3.1	6.8	-4.6	-0.3	-0.5	-2.2
	0.030	44.5	25.9	41.3	32.3	4.8	4.8	6.5	6.8	-6.2	-0.3	0.0	-2.2

Notation

Symbol	Description
f_o	Value at the shoreline
f_r	Value at the extent of inundation
f_h	Value corresponding to flow depth
f_U	Value corresponding to velocity
f_M	Value corresponding to momentum flux
f_{MHW}	Value referenced to MHW datum
f_{max}	Maximum value

Symbols

Symbol	Description	Units
AE	Absolute error	-
c	Empirical coefficient	-
E	Energy	L
e	Error	-
F_r	Froude number	-
g	Acceleration of gravity	LT^{-2}
h	Flow depth	L
k	Gauckler–Manning coefficient conversion factor	$L^{1/3}T^{-1}$
M	Momentum Flux	L^3T^{-2}
MAE	Mean absolute error	-
m	Profile slope	-
n	Gauckler–Manning coefficient	-
p	Pressure	$ML^{-1}T^{-2}$
MRAE	Mean relative absolute error	-
S	Slope of the hydraulic grade line	-
U	Total velocity	LT^{-1}
x	Horizontal distance measure inland from shoreline	L
z	Vertical elevation of land, z = 0 at MHW datum	L
ρ	Density	ML^{-3}

References

ASCE 7. *Minimum Design Loads for Buildings and Other Structures.* Reston, Virginia: American Society of Civil Engineers.

Bryant, E. (2008). *Tsunami: The Underrated Hazard (Second Edition).* Chichester, UK: Springer in association with Praxis.

Carrier, G. F., & Greenspan, H. P. (1958). Water waves of finite amplitude on a sloping beach. *Journal of Fluid Mechanics*, 4 (1), 97-109.

Carrier, G. F., Wu, T. T., & Yeh, H. (2003). Tsunami run-up and draw-down on a plane beach. *Journal of Fluid Mechanics*, 475, 79-99.

Chanson, H. (2006). Tsunami Surges On Dry Coastal Plains: Application Of Dam Break Wave Equations. *Coastal Engineering Journal* , Vol. 48, No. 4, pp. 355-370.

Chow, V. T. (1959). *Open-Channel Hydraulics.* New York: McGraw-Hill Book Company.

Cox, J. C., & Machemehl, J. (1986). Overload Bore Propagation Due to an Overtopping Wave. *Journal of Waterway, Port, Coastal, and Ocean Engineering* , 112, 161-163.

FEMA P646. (2008). *Guidelines for Design of Structures for Vertical Evacuation from Tsunamis.* Washington, D.C., USA: Federal Emergency Management Agency.

French, J. (1982). *Special Computation Procedure Developed for Wave Runup Analysis for Casco Bay, FIS - Maine, 9700-153.* Camp Dresser & McKee.

Kaiser, G., Scheele, L., Kortenhaus, A., Løvholt, F., Römer, H., & Leschka, S. (2011). The influence of land cover roughness on the results of high resolution tsunami inundation modeling. *Natural Hazards and Earth System Sciences* , 2521-2540.

Li, Y., & Raichlen, F. (2003). Energy Balance Model for Breaking Solitary Wave Runup. *Journal of Waterway, Port, Coastal, and Ocean Engineering* , 129(2), 47–59.

Lukkunaprasit, P., Ruangrassamee, A., & Thanasisathit, N. (2009). Tsunami Loading on Buildings with Openings. *Science of Tsunami Hazards* , Vol. 28, No. 5, pp. 303-310.

Lynett, P. J., Liu, P. L., Sitanggang, K. I., & Kim, D. (2008). *Modeling Wave Generation, Evolution, and Interaction with Depth-Integrated, Dispersive Wave Equations COULWAVE Code Manual Cornell University Long and Intermediate Wave Modeling Package.* Cornell University.

Madsen, P. A., & Schaffer, H. A. (2010). Analytical solutions for tsunami runup on a plane beach; single waves, N-waves and transient waves. *Journal of Fluid Mechanics* , 645, 27-57.

Madsen, P. A., Fuhrman, D. R., & Schäffer, H. A. (2008). On the solitary wave paradigm for tsunamis. *Journal of Geophysical Research* , 113, 22 pages.

Mori, N., & Takahashi, T. (2012). Post Event Survey and Analysis of the 2011 Tohoku Earthquake Tsunami. *Coastal Engineering Journal* , Vol. 54, No. 1, 27 pages.

National Tsunami Hazard Mitigation Program. (2012). Proceedings and Results of the 2011 NTHMP Model Benchmarking Workshop. Boulder, CO: Department of Commerce/NOAA/NTHMP; (NOAA Special Report). 436 p.

Pimanmas, A., Joyklad, P., & Warnitchai, P. (2010). Structural Design Guideline for Tsunami Evacuation Shelter. *Journal of Earthquake and Tsunami* , 4 (4).

PMEL. (2006). *Method of Splitting Tsunami (MOST) Software Manual.* NOAA.

Priest, G. R. (1995). *Explanation of Mapping Methods and use of the Tsunami Hazard Maps of the Oregon Coast.* Portland, Oregon: Department of Geology and Mineral Industries, Open-File Report O-95-67.

Rouse, H. (1946). *Elementary Mechanics of Fluids.* New York: Dover Publications, Inc.

Shen, M. C., & Meyer, R. E. (1963). Climb of a bore on a beach Part 3. Run-up. *Journal of Fluid Mechanics* , Vol. 16, Iss. 01, pp. 113-125.

Shi, F., Kirby, J. T., Harris, J. C., Geiman, J. D., & Grilli, S. T. (2012). A high-order adaptive time-stepping TVD solver for Boussinesq modeling of breaking waves and coastal inundation. *Ocean Modelling* , 43–44 (2012) 36–51.

Shi, F., Kirby, J. T., Tehranirad, B., & Harris, J. C. (2011). *FUNWAVE-TVD, documentation and users' manual.* Newark, Delaware: University of Delaware.

Shi, F., Kirby, J. T., Tehranirad, B., Harris, J. C., & and Grilli, S. (2012). *FUNWAVE-TVD Fully Nonlinear Boussinesq Wave Model with TVD Solver Documentation and User's Manual, Version 2.0.* Newark, Delaware: Center for Applied Coastal Research, University of Delaware.

Synolakis, C. E. (1987). The Runup of Solitary Waves. *Journal of Fluid Mechanics* , 185, 523-545.

Tehranirad, B., Shi, F., Kirby, J. T., Harris, J. C., & Grilli, S. (2011). *Tsunami benchmark results for fully nonlinear Boussinesq wave model FUNWAVE-TVD, Version 1.0.* Newark, Delaware: Center for Applied Coastal Research, University of Delaware.

Wamsley, T. V., Cialone, M. A., Smith, J. M., Atkinson, J. H., & Rosati, J. D. (2010). The potential of wetlands in reducing storm surge. *Ocean Engineering* , 59-68.

Wei, G., & Kirby, J. T. (1995). Time-dependent numerical code for extended Boussinesq equations. *Journal of Waterway, Port, Coastal, and Ocean Engineering* , 121 (5): 251–261.

Wei, G., Kirby, J. T., Grilli, S., & Subramanya, R. (1995). A fully nonlinear Boussinesq model for free surface waves. Part 1: highly nonlinear unsteady waves. *Journal of Fluid Mechanics* , 294:71–92.

Willmott, C. J., & Matsuura, K. (2005). Advantages of the mean absolute error (MAE) over the root mean square error (RMSE) in assessing average model performance. *Climate Research* , Vol. 30, pp 79-82.

Yeh, H. (2006). Maximum Fluid Force in the Tsunami Runup Zone. *Journal of Waterway, Port, Coastal, and Ocean Engineering* , 132, 496-500.

Zhang, H., Madsen, O. S., Sannasiraj, S. A., & Chan, E. S. (2004). Hydrodynamic model with wave–current interaction in coastal regions. *Estuarine, Coastal and Shelf Science* , 317–324.